CERN-THESIS-2024-231
13/11/2024

Bachelor Thesis

A comprehensive analysis of an eddy current septum magnet used for top-up beam injection in the upcoming SOLEIL II particle accelerator upgrade

by Jonathan Plett
Matr.-Nr. 421397

This work was submitted to the Institute of High Frequency Technology.

Supervised by:
Prof. Dr.-Ing. Dirk Heberling
Miroslav Atanasov (CERN)

Bachelor Thesis
Aachen,
12 November 2024

Bachelor Thesis

A comprehensive analysis of an eddy current septum magnet used for top-up beam injection in the upcoming SOLEIL II particle accelerator upgrade

by Jonathan Plett, Matriculation Number 421397

RWTH Aachen University
Institute of High Frequency Technology
Prof. Dr.-Ing. Dirk Heberling
Melatener Str. 25
52074 Aachen
Telephone +49 241 80-27932
Fax +49 241 80-22641
www.ihf.rwth-aachen.de
post@ihf.rwth-aachen.de

Eidesstattliche Versicherung

Statutory Declaration in Lieu of an Oath

Jonathan Plett
Name, Vorname/Last Name, First Name

421397
Matrikelnummer/Matriculation No.

Ich versichere hiermit an Eides Statt, dass ich die vorliegende Bachelorarbeit mit dem Titel I hereby declare in lieu of an oath that I have completed the present Bachelor thesis entitled

A comprehensive analysis of an eddy current septum magnet used for top-up beam injection in the upcoming SOLEIL II particle accelerator upgrade

selbstständig und ohne unzulässige fremde Hilfe (insbes. akademisches Ghostwriting) erbracht habe. Ich habe keine anderen als die angegebenen Quellen und Hilfsmittel benutzt. Für den Fall, dass die Arbeit zusätzlich auf einem Datenträger eingereicht wird, erkläre ich, dass die schriftliche und die elektronische Form vollständig übereinstimmen. Die Arbeit hat in gleicher oder ähnlicher Form noch keiner Prüfungsbehörde vorgelegen.
independently and without illegitimate assistance from third parties (such as academic ghostwriters). I have used no other than the specified sources and aids. In case that the thesis is additionally submitted in an electronic format, I declare that the written and electronic versions are fully identical. The thesis has not been submitted to any examination body in this, or similar, form.

Aachen, 12 November 2024
Ort, Datum/City, Date

J. Plett
Unterschrift/Signature

Belehrung:
Official Notification:

§ 156 StGB: Falsche Versicherung an Eides Statt
Wer vor einer zur Abnahme einer Versicherung an Eides Statt zuständigen Behörde eine solche Versicherung falsch abgibt oder unter Berufung auf eine solche Versicherung falsch aussagt, wird mit Freiheitsstrafe bis zu drei Jahren oder mit Geldstrafe bestraft.

Para. 156 StGB (German Criminal Code): False Statutory Declarations
Whoever before a public authority competent to administer statutory declarations falsely makes such a declaration or falsely testifies while referring to such a declaration shall be liable to imprisonment not exceeding three years or a fine.

§ 161 StGB: Fahrlässiger Falscheid; fahrlässige falsche Versicherung an Eides Statt
(1) Wenn eine der in den §§ 154 bis 156 bezeichneten Handlungen aus Fahrlässigkeit begangen worden ist, so tritt Freiheitsstrafe bis zu einem Jahr oder Geldstrafe ein.
(2) Straflosigkeit tritt ein, wenn der Täter die falsche Angabe rechtzeitig berichtigt. Die Vorschriften des § 158 Abs. 2 und 3 gelten entsprechend.

Para. 161 StGB (German Criminal Code): False Statutory Declarations Due to Negligence
(1) If a person commits one of the offences listed in sections 154 through 156 negligently the penalty shall be imprisonment not exceeding one year or a fine.
(2) The offender shall be exempt from liability if he or she corrects their false testimony in time. The provisions of section 158 (2) and (3) shall apply accordingly.

Die vorstehende Belehrung habe ich zur Kenntnis genommen:
I have read and understood the above official notification:

Aachen, 12 November 2024
Ort, Datum/City, Date

J. Plett
Unterschrift/Signature

Abstract

Particle accelerators are used to conduct scientific experiments in numerous fields like fundamental physics or medicine, amongst others. Charged particles are accelerated to high energies employing multiple accelerator stages. This necessitates the extraction and injection of the particle beam to navigate the particles between the different stages. Both injection and extraction require numerous systems to ensure that the particle beam follows the desired trajectory, and one of these systems is the septum magnet. A collaboration between CERN (European Organisation for Nuclear Research) and SOLEIL (Source optimisée de lumière d'énergie intermédiaire du LURE) has been established to analyse a fast pulsed, thin eddy-current septum magnet that was designed for the Top-Up injection of the SOLEIL II accelerator upgrade. The requirements for this device regarding its magnetic characteristics are challenging. In this thesis, a comprehensive magnetic study of the eddy-current septum magnet is carried out using detailed finite element simulation. A particular focus lies on the magnetic shielding performance of the septum blade down to the micro-Tesla level to ensure a stable operation of the SOLEIL II accelerator.

Kurzfassung

Teilchenbeschleuniger werden in zahlreichen wissenschaftlichen Bereichen wie der physikalischen Grundlagenforschung oder der Medizin für Experimente genutzt. Geladene Teilchen werden mittels mehrerer Beschleunigungsstufen auf hohe Energien gebracht. Dies erfordert die Extraktion und Injektion des Teilchenstrahls, um die Teilchen zwischen den verschiedenen Stufen zu navigieren. Sowohl Injektion als auch Extraktion benötigen verschiedene Systeme, um sicherzustellen, dass der Teilchenstrahl die gewünschte Trajektorie einhält. Eines dieser Systeme ist der Septum Magnet.
In einer Kollaboration zwischen CERN (Europäische Organisation für Kernforschung) und SOLEIL (Source optimisée de lumière d'énergie intermédiaire du LURE) wird ein solcher Septum Magnet untersucht, welcher für die Top-Up Injektion im Rahmen des SOLEIL-II Beschleuniger Upgrades entwickelt wurde. In dieser Arbeit wird eine Analyse des Wirbelstrom-Septummagneten mit Finite-Elemente-Simulationen hinsichtlich seiner magnetischen Eigenschaften durchgeführt. Ein besonderer Fokus liegt dabei auf der magnetischen Abschirmqualität bis zum mikro-Tesla Bereich, um einen stabilen Betrieb des SOLEIL-II Beschleunigers sicherzustellen.

Contents

1 Introduction **1**

2 Background **2**
2.1 Eddy-Current Septum Magnet . . . 2
2.2 Electromagnetism . . . 3
2.3 Magnetic Field - Harmonics . . . 5
2.4 Beam Deflection in a Dipole Field . . . 7
2.5 Beam Deflection in a Quadrupole Field . . . 9
2.6 Simulation Software - Opera® . . . 9

3 Analysis of an Eddy-Current Septum Magnet for SOLEIL II **10**
3.1 Design Specifications . . . 10
3.2 Main Field . . . 12
3.2.1 Main Field Integral . . . 12
3.2.2 Main Field Homogeneity . . . 12
3.3 Leakage Field . . . 15
3.3.1 Simulation Approach . . . 16
3.3.2 Copper Shielding and Validation of the Simulation Approach . . . 17
3.3.3 μ-Metal and Copper Shielding . . . 22
3.3.4 Steel and Copper Shielding . . . 27
3.3.5 Comparison . . . 28
3.3.6 Outlook - Faster pulsing . . . 29
3.4 Simulations - Discussion . . . 31

4 Benchmarking **32**
4.1 SMH16-CF Measurement . . . 32
4.2 SOLEIL I - Spare Eddy-Current Septum Magnet . . . 37
4.3 Benchmarking - Discussion . . . 39

5 Conclusion and Outlook **41**

A Appendix **42**

Bibliography **49**

List of Figures

1.1 Schematic overview of an injection scheme using a septum magnet 1

2.1 Cross-section of the SOLEIL II eddy-current septum magnet 2
2.2 Longitudinal cross-section the SOLEIL II eddy-current septum magnet (not to scale) 3
2.3 BH-characteristic for ferromagnetic steel 4
2.4 Induction of eddy-currents due to a time-varying magnetic field 4
2.5 **Magnetic quadrupole**
The two-dimensional magnetic field of a quadrupole is shown: $\vec{B}(x, y) = (x, y)^T$. The magnitude of the magnetic field, indicated by the color, is normalized by the maximum value. 6
2.6 Motivation of equation 2.3.3 to calculate the magnetic harmonics 7
2.7 Sketch of the deflection of an electron beam in the field of a magnetic dipole 8

3.1 **Current excitation of the SOLEIL II eddy-current septum magnet**
50 μs full sine pulse with a peak current of 4000 A 10
3.2 Dimensions and location of the Good Field Region (GFR) 11
3.3 Main deflection field at the point of injection (t = 12.5 μs) as a function of position (blue) and a simplification as a rectangle function with the same main field integral (red) 12
3.4 Schematic overview of shims that improve the uniformity of the deflection field (not to scale) 13
3.5 Homogeneity of the magnetic deflection field in the GFR at the time of injection (t = 12.5 μs) with and without shims (the colors correspond to different values in both graphs) 13
3.6 Dependency of the homogeneity $\mathcal{H}_1$ of the magnetic deflection field on the width and height of the shim 14
3.7 Set of dimensions of the shim that improve the homogeneity of the main field to below 10^{-3} 14
3.8 **Necessary meshing to properly model the skin-effect**
The figure shows the decay of the magnetic field B in a conducting material in the first three skin-depth (δ) layers. It illustrates how this field-gradient must be meshed to guarantee accurate results. 16
3.9 **Sketch of the simulations approach**
The simulation is split up into three parts. The magnet's ends are simulated with three-dimensional simulations and the magnet's center is simulated with 26 two-dimensional simulations. 17
3.10 Sketch of the simulation approach (as is also shown in Fig. 3.9) for a version of the septum magnet with only copper-shielding and simplified ends . . . 18
3.11 **Transient three-dimensional simulation for a simplified version of the magnet**
The plot shows the magnetic leakage field at the position of the stored beam (z-axis) as a function of time. 19

3.12 **Transient three-dimensional simulation of the magnet's ends for a simplified version of the magnet**
The plot shows the magnetic leakage field at the position of the stored beam (z-axis) as a function of time for both ends. 20
3.13 **26 Transient two-dimensional simulations of the magnet's center for a simplified version of the magnet**
The plot shows the magnetic leakage field at the position of the stored beam (z-axis) as a function of time for the central part of the magnet. . . . 20
3.14 **Reconstructed magnetic leakage field for a simplified version of the magnet**
The simulations from Fig. 3.11 and 3.13 are combined to reconstruct the leakage field of the complete model. 21
3.15 Comparison of the leakage field integral of a simplified magnet between the reconstruction comprising two-dimensional and three-dimensional simulations and a complete three-dimensional simulation 22
3.16 Manually generated BH-curves for μ-metal at different initial permeabilities μ_r^{init} 23
3.17 **Reconstructed magnetic leakage field for a two-layer septum blade comprising copper and μ-metal with a permeability of μ-metal of $\mu_r^{init} = 10^3$**
The plot shows the magnetic leakage field at the position of the stored beam (z-axis) as a function of time. 24
3.18 **Leakage field integral for a two-layer septum blade comprising copper and μ-metal**
The plot shows the leakage field integral as a function of time for two different BH-curves of μ-metal. Each dot corresponds to the value of one simulated time-step. These are connected linearly. 25
3.19 **Integrated quadrupole component for a two-layer septum blade comprising copper and μ-metal**
The plot shows the integrated quadrupole component as a function of time for two different BH-curves of μ-metal. Each dot corresponds to the value of one simulated time-step. These are connected linearly. 26
3.20 **Dependency of the leakage field on the relative permeability**
The maximum value of the leakage field is plotted as a function of the permeability of μ-metal for two different thicknesses of copper in the septum blade. 27
3.21 Manually generated BH-curve for steel with $\mu_r^{init} = 10^2$ and $B_{sat} = 1.92$ T 28
3.22 Integrated dipole and quadrupole fields for a composite septum blade comprising copper and ferromagnetic steel at a permeability of $\mu_r^{init} = 10^2$ . . . 28
3.23 **Kick error for a pulse width of 10 μs**
The blue curve shows the deflection field as a function of time. The injected bunch with a length of 304 ns (indicated in red) is subject to different magnetic field strengths, causing a kick error. 30
3.24 **Leakage field for different excitation frequencies**
The plot shows the leakage field as a function of time five millimeters away from a two-layer septum blade comprising μ-metal and copper for different excitation frequencies. 30
3.25 **Dependency of the leakage field on the excitation frequency**
The plot shows the simulated maximum leakage field as a function of the excitation frequency (blue) and a curve that fits the data (red). 31

4.1 **SMH16-CF cross-section**
A punctual probe is positioned both in the main field gap and 17 mm away from the septum blade. The material of the area that is marked by an orange dotted line is copper in a first measurement and aluminum in a second. 33
4.2 SMH16-CF longitudinal cross-section and positioning of the punctual probe to perform a leakage field scan - only half of the magnet is measured 33
4.3 **Current excitation of SMH16-CF**
640 μs half sine pulse with a peak current of 4976 Amperes 34
4.4 Comparison between measurement and simulation of the main magnetic field of the SMH16-CF 34
4.5 **Measurement of the leakage field of SMH16-CF with a copper septum**
Each line corresponds to one measurement of the magnetic field at one position along the longitudinal axis of the magnet. 35
4.6 **Simulation of the leakage field of SMH16-CF with a copper septum**
Each line corresponds to one simulated time step that is reconstructed from two-dimensional and three-dimensional simulations. 36
4.7 Comparison of the leakage field integral of SMH16-CF with a copper septum blade between simulation and measurement 36
4.8 Comparison of the leakage field integral of SMH16-CF with an aluminum septum blade between simulation and measurement 37
4.9 Cross-section of the SOLEIL I spare septum magnet 38
4.10 SOLEIL spare septum magnet longitudinal cross-section and positioning of the integral probe to perform a leakage field measurement 38
4.11 **Current excitation of the SOLEIL eddy-current spare magnet**
140 μs full sine pulse with a peak current of 4921 Amperes 38
4.12 Comparison of the leakage field integral between measurement and simulation for the SOLEIL spare septum magnet 39

A.1 **A complete three-dimensional view of the SOLEIL II eddy-current septum magnet**
The injected beam and the stored beam enter the septum magnet on the upstream side. The injected beam is deflected towards the stored beam. . . . 42
A.2 Three-dimensional view of the cross-section of the SOLEIL II eddy-current septum magnet 42
A.3 **Three-dimensional model for the upstream end of the SOLEIL II eddy-current septum magnet**
The cutting-plane is perpendicular to the coil. Therefore, the boundary condition "tangential magnetic field" is imposed on all faces at the cutting-plane. The coil is not part of the mesh and is therefore kept entirely. . . . 43
A.4 **Magnetic dipole**
The two-dimensional magnetic field of a dipole is shwon: $\vec{B}(x,y) = (0,1)^T$. The magnitude of the magnetic field, indicated by the color, is normalized by the maximum value. 44
A.5 **Magnetic sextupole**
The two-dimensional magnetic field of a sextupole is shown: $\vec{B}(x,y) = (2xy, x^2 - y^2)^T$. The magnitude of the magnetic field, indicated by the color, is normalized by the maximum value. 45

A.6 **Magnetic octupole**
The two-dimensional magnetic field of an octupole is shown: $\vec{B}(x, y) = (3yx^2 - y^3, x^3 - 3xy^2)^T$. The magnitude of the magnetic field, indicated by the color, is normalized by the maximum value. 46
A.7 **Measurement of the leakage field of SMH16-CF with an aluminum septum**
Each line corresponds to one measurement of the magnetic field at one position along the longitudinal axis of the magnet. 47
A.8 **Simulation of the leakage field of SMH16-CF with an aluminum septum**
Each line corresponds to one simulated time step that is reconstructed from two-dimensional and three-dimensional simulations. 47
A.9 CERN accelerator complex [1] 48

List of Tables

3.1 Achieved improvement of the uniformity of the magnetic deflection field by adding shims 14
3.2 Properties of copper, ferromagnetic steel and μ-metal: Conductivity, permeability and skin-depth for a frequency f = 20 kHz 15
3.3 Comparison of the integrated dipole field (Bdl_{DP}) and the integrated quadrupole field (Bdl_{QP}) for different septum blade materials and different material properties 29

4.1 **Comparison between measurement and simulation**
The table shows the peak values of simulation (S) and measurement (M) for different magnets and different excitations. SMH16-CF is pulsed with a half sine pulse (T/2) and the SOLEIL spare septum magnet with a full sine (T). 39

1 Introduction

At the French national synchrotron facility SOLEIL, synchrotron radiation is used as a light source to conduct experiments in fields ranging from biology to condensed matter physics. Synchrotron radiation is created by the centripetal acceleration of electrons in the circular storage ring and provides the experiments with excellent characteristics to study samples on the atomic scale [2]. To achieve a stable operation with a constant beam current and beam intensity, beam losses must be compensated. This is achieved through top-up injection, which involves frequent injections during operation [3]. Here, the septum magnet plays a crucial role, as it deflects the injected beam as close as possible to the stored beam. The merge between the two beams is performed downstream with the use of other pulsed systems. Ideally, the trajectory of the injected beam is diverted towards the stored beam without perturbing the stored beam [4]. This concept is illustrated in Fig. 1.1.

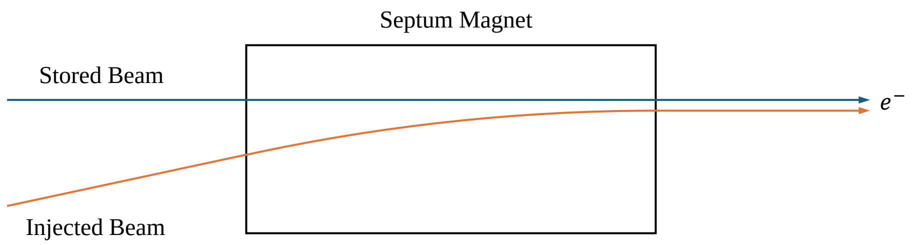

Fig. 1.1: Schematic overview of an injection scheme using a septum magnet

In collaboration with CERN, SOLEIL aims to redesign its top-up injection scheme for its next-generation storage ring of the SOLEIL II accelerator upgrade. A design for a fast pulsed eddy-current septum magnet, that was proposed by the Division Accélérateurs et Ingénierie of SOLEIL, is analysed in this thesis using detailed transient 3D finite element simulation.
This work comprises three main chapters: Chapter 2 provides necessary background information about septum magnets and explains the tools to magnetically analyse them. The next chapter (Chap. 3) shows a detailed study of the eddy-current septum magnet for the SOLEIL II accelerator upgrade. The magnet will be examined with a particular focus on its shielding performance to ensure minimal perturbations of the stored beam. Therefore, a suitable simulation approach will be established and validated to ensure physically valid results. Next, different shielding materials will be tested and the magnet's performance will be evaluated with respect to the challenging restrictions of the septum magnet. In the last chapter (Chap. 4), an attempt is made to magnetically validate the accuracy of the simulations by comparing the measurements of two other septum magnets to the simulations. The obtained results will finally be discussed in chapter 5.

2 Background

2.1 Eddy-Current Septum Magnet

Multiple designs can achieve the desired functionality that was depicted in Fig. 1.1 and explained in chapter 1, and one of these designs is called the eddy-current septum magnet. Figure 2.1 illustrates a cross-sectional view of the eddy-current septum magnet that was designed by the Division Accélérateurs et Ingénierie of SOLEIL [5]. A current in a coil generates a magnetic field that is magnetically conducted to the location of the injected beam via magnetic steel, also referred to as the yoke. The septum blade shields the stored beam, which is located on the opposite side of the septum blade, from this magnetic field to minimize perturbations of the stored beam. Physically, this is because of the induction of eddy-currents in the septum blade (hence the name eddy-current septum magnet) that cause a secondary magnetic field that opposes and therefore reduces the primary field [4]. In this case, the septum blade comprises one layer of copper and one layer of a ferromagnetic material. A copper box surrounds the entire magnet.

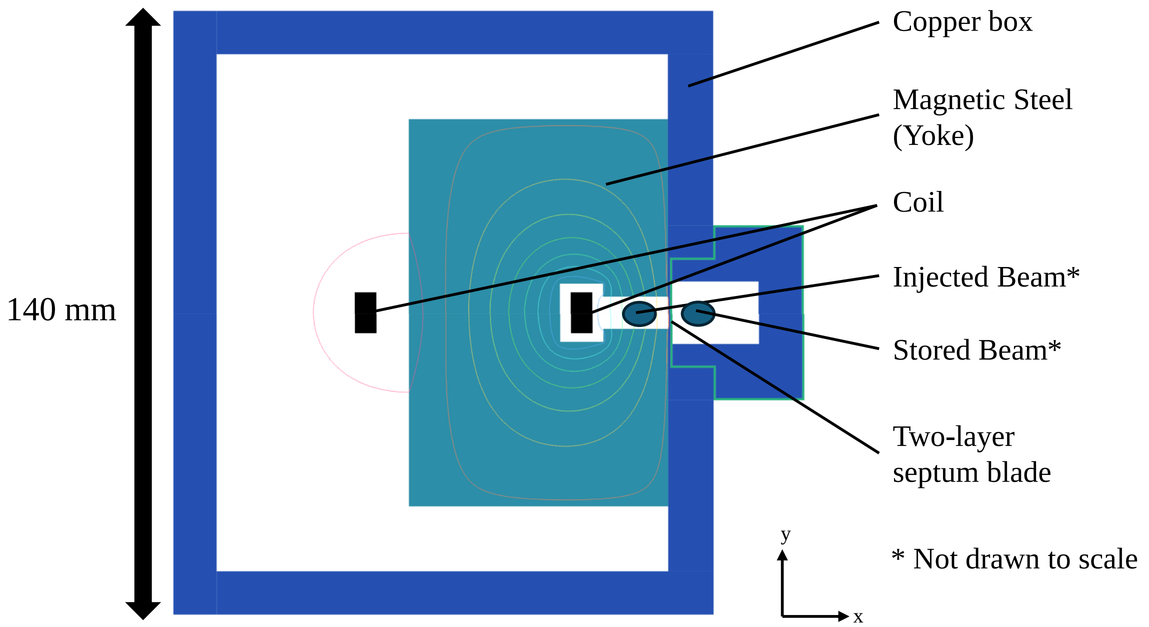

Fig. 2.1: Cross-section of the SOLEIL II eddy-current septum magnet

A longitudinal cross-section is shown in Fig. 2.2 (drawing is not to scale). The injected particle bunch enters the magnet on the left hand side, referred to as the upstream side, and exits the magnet on the right hand side, referred to as the downstream side. The two-layer septum blade decreases in thickness along the longitudinal z-axis from 3.5 mm to 1 mm over a length of 450 mm. It magnetically shields the stored beam, which follows a straight trajectory on the other side of the septum blade. The yoke and the coils are rotated such that they parallel to the septum blade [5]. Three-dimensional views of the septum magnet can be viewed in App. A in Fig. A.1 and Fig. A.2.

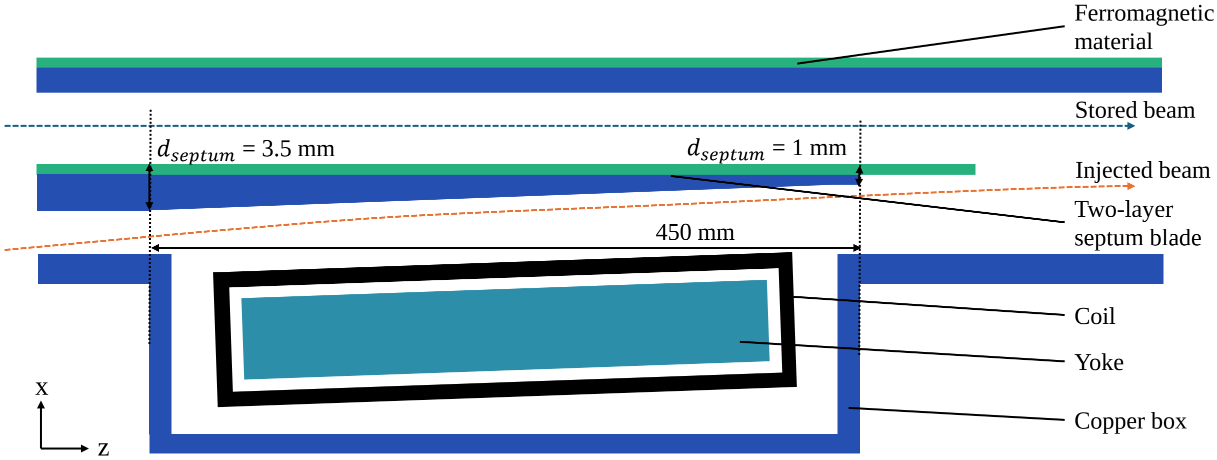

Fig. 2.2: Longitudinal cross-section the SOLEIL II eddy-current septum magnet (not to scale)

2.2 Electromagnetism

A further study of the behaviour of septum magnets necessitates a quick overview of electromagnetism. The behaviour and interaction of electric and magnetic fields is captured by Maxwell's equations:

$$\begin{aligned} \vec{\nabla} \times \vec{H} &= \vec{J} + \frac{\partial \vec{D}}{\partial t} \\ \vec{\nabla} \times \vec{E} &= -\frac{\partial \vec{B}}{\partial t} \\ \vec{\nabla} \cdot \vec{D} &= \frac{\rho}{\epsilon} \\ \vec{\nabla} \cdot \vec{B} &= 0 \end{aligned} \tag{2.2.1}$$

Of particular importance for this thesis are the first two equations. The first equation, referred to as Ampere's law, describes how moving charges ($\vec{J}$) create a magnetic field ($\vec{H}$). The second equation is called the induction law and formulates how a time-varying magnetic flux-density ($\vec{B}$) induces an electric field ($\vec{E}$). The magnetic field-strength $\vec{H}$ and the magnetic flux-density $\vec{B}$ are connected through the permeability μ of the material: $\vec{B} = \mu\vec{H} = \mu_r\mu_0\vec{H}$. For ferromagnetic materials, however, the BH-characteristic is nonlinear and a BH-curve is necessary to capture this nonlinear dependency [6]. Figure 2.3 shows the BH-curve of ferromagnetic steel as an example [7]. In the nonlinear case, the permeability is defined as the derivative of the BH-curve: $\mu(H) = \frac{dB}{dH}$. The initial relative permeability is defined as the derivative of the curve at $H = 0 \, \frac{A}{m}$, normalized by the vacuum permeability (μ_0): $\mu_r^{init} = \frac{1}{\mu_0}\frac{dB}{dH}|_{H=0}$.

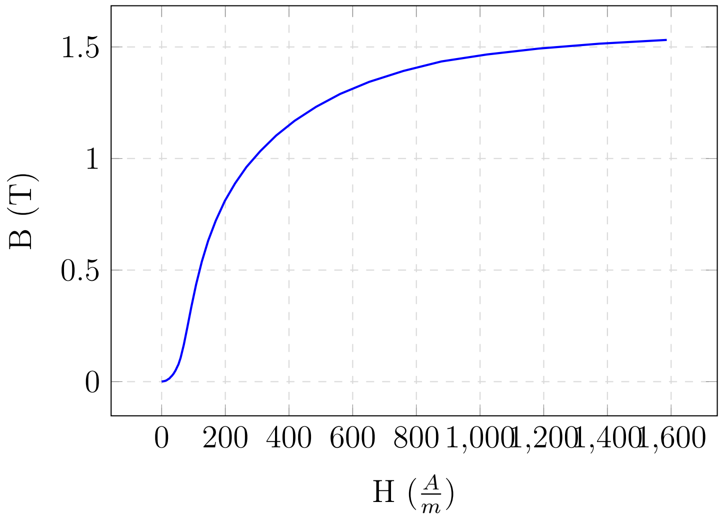

Fig. 2.3: BH-characteristic for ferromagnetic steel

The previous section (Sec. 2.1) already mentioned the reliance of eddy-current septum magnets on the induction of eddy-currents in the septum blade to provide sufficient magnetic shielding for the stored beam in the accelerator ring. This process is sketched in more detail in Fig. 2.4. A material with conductivity σ is subject to a time-varying magnetic field with an increasing magnitude. Consequently, the derivative of the magnetic field with respect to time is positive: $\frac{dB_z}{dt} > 0$. According to the second one of Maxwell's equations (Eq. 2.2.1), an electric field is induced in the conducting material which curls counterclockwise around the z-axis. By Ohm's law ($\vec{J} = \sigma\vec{E}$), a current will flow in the conductive material which then causes a secondary magnetic field by Maxwell's first law (Eq. 2.2.1). This secondary magnetic field opposes the rate of change of the primary magnetic field. This phenomenon is utilized in eddy-current septum magnets as the magnetic field entering the septum blade can be significantly reduced, as long as the rate of change of the primary magnetic field and the conductivity of the material are sufficiently high [6].

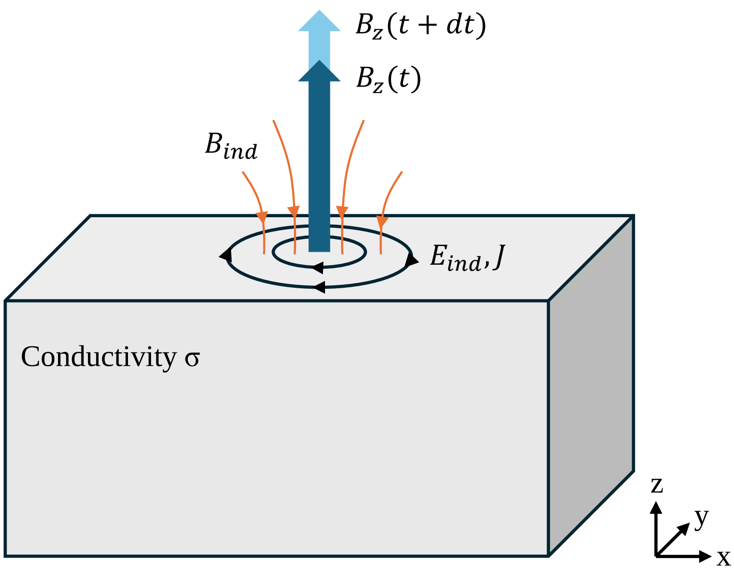

Fig. 2.4: Induction of eddy-currents due to a time-varying magnetic field

2.3 Magnetic Field - Harmonics

A detailed analysis of a magnetic field can be carried out by decomposing it into its harmonic components, which is of importance for later analysis of the magnetic field generated by the septum magnet. With $\vec{e}_x$ pointing horizontally and $\vec{e}_y$ pointing vertically in the cross-section of the septum magnet in Fig. 2.1, the following complex function B can be defined that describes a two-dimensional magnetic field:

$$B(x+iy) = B_y(x+iy) + iB_x(x+iy) \in \mathbb{C}$$

It can be shown with Maxwell's equations that B satisfies the Cauchy-Riemann equations (Eq. 2.3.1), which proves it to be an analytic function [8].

$$\frac{\partial B_y}{\partial x} = \frac{\partial B_x}{\partial y} \quad \& \quad \frac{\partial B_y}{\partial y} = -\frac{\partial B_x}{\partial x} \tag{2.3.1}$$

Every analytical function can be expressed as a complex Taylor series (Eq. 2.3.2). In the case of a magnetic field, every component of this Taylor series corresponds to a magnetic multipole or in other words a magnetic harmonic. For instance, C_0 is the dipole component of the magnetic field, C_1 is the quadrupole component, etc [8]. The quadrupole harmonic is visualized as an example in Fig. 2.5, which shows the two-dimensional magnetic vector field $\vec{B}(x,y) = (B_x(x,y), B_y(x,y))^T$ for the quadrupole component. This field is obtained by setting every C_n of Eq. 2.3.2 to zero except for the quadrupole component C_1, which is set to one. The complex function $B(x+iy)$ can then be viewed as a two-dimensional vector field $\vec{B}$. The dipole, sextupole and octupole field can be viewed in App. A in Fig. A.4, Fig. A.5 and Fig. A.6 respectively.

$$B_y(x+iy) + iB_x(x+iy) = \sum_{n=0}^{\infty} C_n \cdot (x+iy)^n \quad C_n \in \mathbb{C} \tag{2.3.2}$$

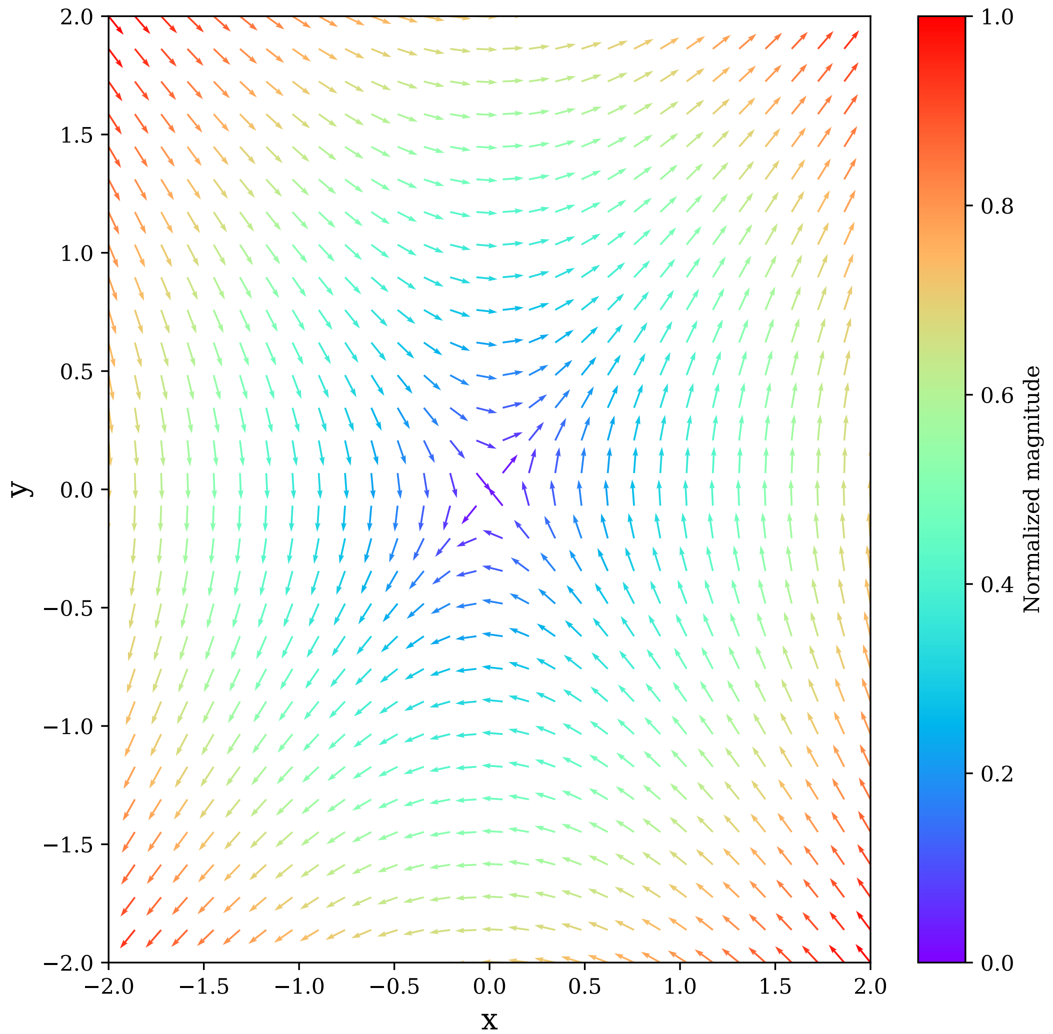

Fig. 2.5: **Magnetic quadrupole**
The two-dimensional magnetic field of a quadrupole is shown: $\vec{B}(x,y) = (x,y)^T$. The magnitude of the magnetic field, indicated by the color, is normalized by the maximum value.

These harmonics can be obtained using Eq. 2.3.3, where B_t is the field tangential to the circumference of a circle with radius R [9].

$$C_n = \frac{1}{\pi R^n} \int_0^{2\pi} B_t(\phi) e^{-i(n+1)\phi} d\phi \tag{2.3.3}$$

This equation can be motivated using Fig. 2.6. The right hand side plots the magnetic field that is tangential to the circumference of a circle with radius R as a function of the angle ϕ. The magnetic field is shown on the left hand side, in this case the field of a perfect dipole is chosen as an example. The magnetic field tangential to the circumference of the circle is obtained by calculating the scalar-product between a unit-vector that is tangential to the circumference and the magnetic field at that position: $B_t = \vec{e}_t(R,\phi) \cdot \vec{B}(R,\phi)$. The resulting function $B_t(\phi)$ for the case of a magnetic dipole is a perfect cosine with a period T = 2π, whereas a quadrupole field results in a cosine with a period T = π, etc. Consequently, a Fourier Transform can be used to extract the harmonic components C_n of the magnetic field $\vec{B}$.

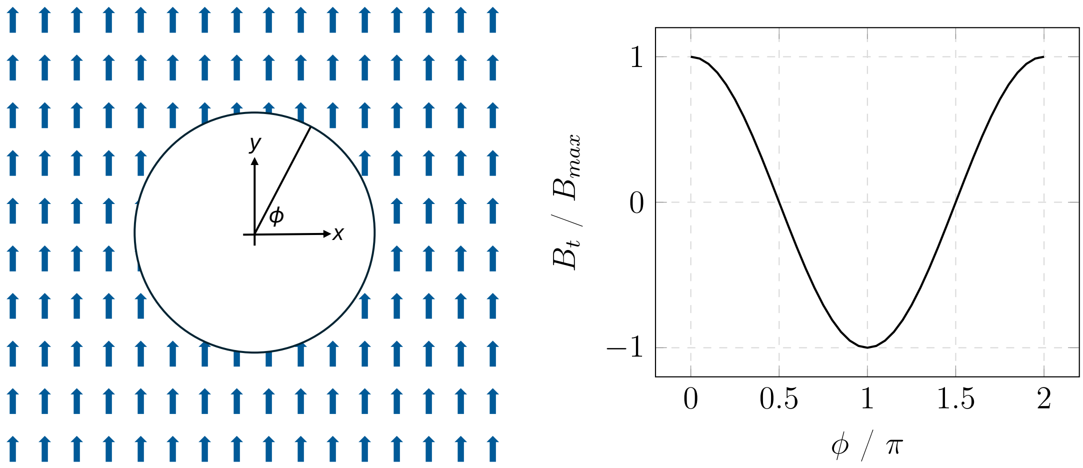

Fig. 2.6: Motivation of equation 2.3.3 to calculate the magnetic harmonics

Furthermore, another metric $\mathcal{H}_1$ is defined to quantify the homogeneity of any given magnetic field in a domain D (Eq. 2.3.4). It gives the maximum deviation of the magnetic field in the domain D from the dipole component B_{Dipole} (which corresponds to C_0 in Eq. 2.3.2), normalized by the dipole component:

$$\mathcal{H}_1 = \frac{1}{B_{Dipole}} max_{\vec{x} \in D} |B(\vec{x}) - B_{Dipole}| \tag{2.3.4}$$

The next two sections explain how the different magnetic harmonics affect a particle beam that passes through them.

2.4 Beam Deflection in a Dipole Field

A magnetic field is generated by the current in the coil of the septum magnet by Amperes law (Eq. 2.2.1) in order to deflect the injected beam such that it comes as close as possible to the stored beam. The merge between the two beams is done further downstream by other pulsed systems. In general, the Lorentz force describes the force on a charged particle due to the presence of electric and magnetic fields:

$$\vec{F_L} = q(\vec{E} + \vec{v} \times \vec{B})$$

Therefore, an electric field could also be used for beam injection. However, for high energies and a velocity v $\approx$ c, an electric field of about $3 \cdot 10^8 \ \frac{V}{m}$ would be needed to obtain the same force as a magnetic field of just 1 T. Electric fields of this magnitude are impractical and only field strengths of just over $10^7 \ \frac{V}{m}$ can be stably achieved. This explains the usage of magnets for injection and extraction purposes at high beam energies. Electrostatic septa can be used at lower beam energies with the advantage of less energy consumption.

The deflection process in a magnetic field is sketched in Fig. 2.7. Here, an electron-beam comes from the top right corner and is bent by an angle θ due to the presence of magnetic dipole field $\vec{B}$, which points out of the plane in this case.

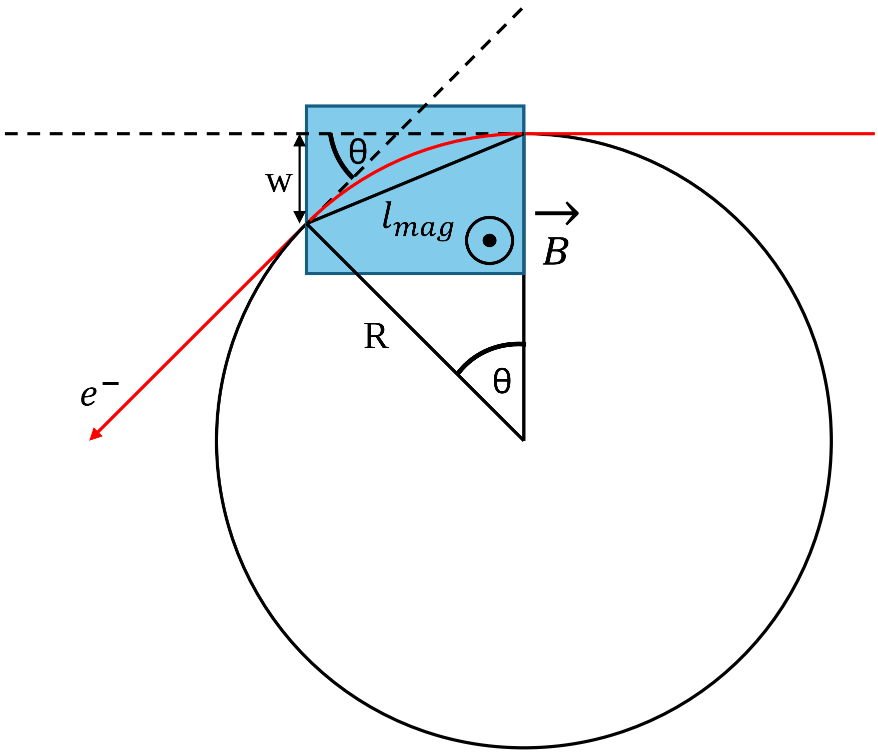

Fig. 2.7: Sketch of the deflection of an electron beam in the field of a magnetic dipole

To find a relation between the deflection angle θ, the magnetic field $\vec{B}$ and the magnetic length l_{mag}, relativistic mechanics need to be used as the particle speed $\vec{v}$ can be close to the speed of light [10]. The particle beam traces a circular arc with radius R in the region where the magnetic field is present (marked in blue). Here, the Lorentz force equals the centripetal force:

$$F_L = F_z \Leftrightarrow q \cdot B \cdot v = \gamma m \frac{v^2}{R}$$

with the relativistic factor $\gamma = \frac{1}{\sqrt{1-\frac{v^2}{c^2}}}$. This results in an expression for the radius R:

$$R = \frac{\gamma m v}{Bq}$$

Next, the following equation can be obtained using simple trigonometry: $sin(\frac{\theta}{2}) = \frac{l_{mag}}{2R}$. As the angle θ is in the range of a few of milli-radians (2.7 is not to scale), the small angle approximation ($sin(\theta) \approx \theta$) can be used to get the dependency of θ on the magnetic field and the magnetic length [10]:

$$\theta = \frac{l_{mag} B q}{\gamma m v} = \frac{Bdl_{main} q}{\gamma m v} \tag{2.4.1}$$

The product $l_{mag} \cdot B$ is referred to as the main field integral, denoted by Bdl_{main}. This magnetic field integral can also be calculated for non-homogeneous fields by integrating the magnetic field along the direction of beam-travel, which is usually defined as the z-axis (Eq. 2.4.2). As the component of the magnetic field parallel to the trajectory of the particle does not cause a Lorentz-force, only the perpendicular component $B_\perp$ needs to be integrated. This integration can also be done along the trajectory of the stored beam, where the fields are ideally as low as possible. This is then referred to as the leakage field integral, denoted by Bdl_{leak}.

$$Bdl = \int B_{\perp}(z) \cdot dz \tag{2.4.2}$$

For non-homogeneous fields the magnetic length is defined as $l_{mag} = \frac{Bdl_{main}}{B_0}$, with B_0 being the magnetic field in the center of the magnet.
The width w that the beam traverses in the magnetic field in the plane of deflection can also be expressed in terms of the deflection angle θ:

$$w = l_{mag} \cdot sin(\frac{\theta}{2}) \approx l_{mag} \cdot \frac{\theta}{2} \tag{2.4.3}$$

This value is used to define a Good Field Region (GFR), which is a domain within the magnet with a homogeneous magnetic field, according to the metrics that were defined in Sec. 2.3.

2.5 Beam Deflection in a Quadrupole Field

A perfect quadrupole field can be obtained mathematically by setting the quadrupole-component from Eq. 2.3.2 to $C_1 = \mathrm{g} > 0 \in \mathbb{R}$, while all other components C_n are set to zero. The resulting field is $\vec{B}_{QP}$, which was already visualized in Fig. 2.5.

$$\vec{B}_{QP} = (B_x, B_y, B_z)^T = (gy, gx, 0)^T$$

An electron beam sitting at $(x, y) = (0, 0)$ and traveling with velocity v in the $\vec{e_z}$-direction will experience a Lorentz Force if it gets displaced from the $\vec{e_z}$-Axis. The resulting force is the following:

$$\vec{F} = -e(\vec{v} \times \vec{B}_{QP}) = ev(B_y, -B_x, 0)^T = ev(gx, -gy, 0)^T$$

Here, it can be seen that a displacement from the z-axis in the y-direction by Δy causes a force $F_y = -evg\Delta y$, which acts against the displacement and therefore steers the beam back towards the z-axis. A displacement in the x-Direction on the other hand causes a force $F_x = evg\Delta x$, which is a positive force that further defocuses the beam. In summary, a quadrupole magnet focuses the beam in one direction, while it defocuses the beam in the other direction. Hence, the quadrupole-harmonic should be minimized for any septum magnet as to not increase the cross-sectional area of the particle beam [10].

2.6 Simulation Software - Opera®

The software that is used to execute all magnetic simulations of chapter 3 and chapter 4 is called Opera® 2024 SP1 by Dassault Systemes. It can simulate and solve static, harmonic and transient electromagnetic models amongst others in both two- and three dimensions. This software is based on the finite element method, in which the partial differential equations that define an electromagnetic problem are approximated by splitting up the domain into a finite number of elements. The continuous time-domain is similarly reduced to a finite number of time steps for transient physical problems. This way, the partial differential equations can be transformed into a system of linear equations, which can then be solved using numerical methods [11].

3 Analysis of an Eddy-Current Septum Magnet for SOLEIL II

This chapter aims to study the SOLEIL II eddy-current septum magnet in detail. First, the design specifications will be presented that ensure that the beam-dynamics requirements are met. After, the magnet will be analyzed with respect to these design specifications using transient finite element simulations.

3.1 Design Specifications

Current

The septum magnet is pulsed with one full sine wave with a period of 50 μs and a peak value of 4 kA, as is shown in Fig. 3.1. This current is carried by the coil that can be seen in the cross-section in Fig. 2.2, and produces a magnetic field which deflects the injected particle beam. The particle bunch is injected at 12.5 μs, i.e. at peak current [5].

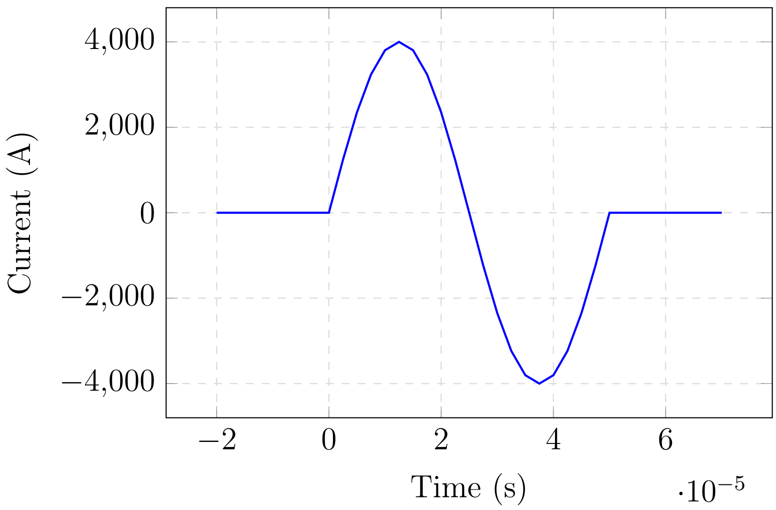

Fig. 3.1: **Current excitation of the SOLEIL II eddy-current septum magnet**
50 μs full sine pulse with a peak current of 4000 A

Septum Blade

The septum blade shields the stored beam from the main magnetic field in the gap. The proposed design has a tapered blade that decreases in thickness from 3.5 mm to 1 mm along the z-axis going towards the downstream side of the magnet (as shown in Fig. 2.2). The septum blade consists of two layers with an outer layer of ferromagnetic material that has a constant thickness of 0.5 mm, and an inner layer of copper that decreases in thickness from 3 mm to 0.5 mm. Eddy-currents are induced in both materials due to the time-varying fields to magnetically shield the stored beam [5].

Deflection Field and Good Field Region

The injection scheme requires the septum magnet to have a nominal deflection angle of $\theta_{nom} = 20$ mrad [5]. Using Eq. 2.4.1, the main field integral required for this angle (Eq. 2.4.2) at a beam energy of 2.75 GeV can be calculated to be $Bdl_{main} = 183.3$ mTm. With a magnetic yoke length of 400 mm, the required magnetic field is $B_{nom} = 0.458$ T, assuming a homogeneous field along the direction of beam travel for the entire yoke length. In the plane of beam deflection, w (Eq. 2.4.3) corresponds to the horizontal width of the GFR and can be evaluated to be less than 8 mm, with the beam not coming closer than 0.1 mm to the septum blade. The vertical height of the GFR is defined to be two millimeters, which is chosen to be larger than the beam diameter of one millimeter. The coordinate system is defined such that the septum blade (see Fig. 2.1) starts at x = -0.5 mm, the coordinates for the GFR for one cross-section are therefore as described in Eq. 3.1.1 and as shown in Fig. 3.2. Within this domain, the requirement $\mathcal{H}_1 \leq 10^{-3}$ (Eq. 2.3.4) is imposed to get an acceptable homogeneity for the main magnetic field [5].

$$GFR := \{(x, y) \in \mathbb{R}^2 : -8.6 \leq \frac{x}{mm} \leq -0.6 \;\;\&\;\; -1.0 \leq \frac{y}{mm} \leq 1.0\} \tag{3.1.1}$$

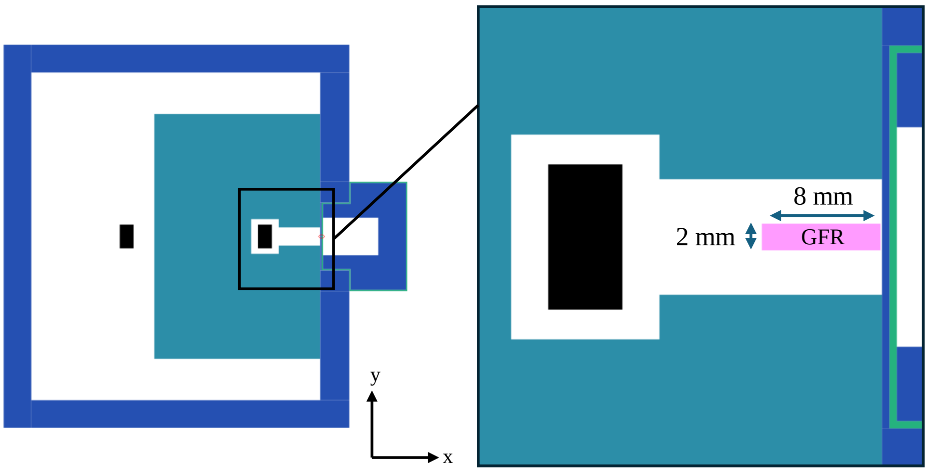

Fig. 3.2: Dimensions and location of the Good Field Region (GFR)

Leakage Field

The magnetic field that is seen by the stored beam on the back-side of the septum blade is referred to as the leakage field, stray field or residual field. The integrated dipole component (C_0) of the leakage field, also referred to as the leakage field integral, should be minimal to reduce perturbations of the stored beam. Ideally, the integrated leakage field (Eq. 2.4.2) should be lower than 10 μTm: $Bdl_{leakage} = \int C_0(z)dz \leq 10$ μTm. The ratio between leakage field and main field integral that quantifies the shielding performance is consequently in the order of magnitude 10^{-5}: $\frac{Bdl_{leak}}{Bdl_{main}} \propto 10^{-5}$ [5].
The quadrupole component (C_1) should not exceed 0.05 $\frac{T}{m}$ to prevent a defocusing of the stored beam. The integrated quadrupole component should therefore be less than 0.02 $\frac{T}{m}m$: $Bdl_{leak,QP} = \int C_1(z)dz \leq 0.02$ $\frac{T}{m}m$ [5].

3.2 Main Field

The main deflection field has the purpose to deflect the injected beam towards the stored beam. As explained in the previous section, the main field integral (Eq. 2.4.2) should have a value of 183.3 mTm for nominal deflection. The main field and its homogeneity is analyzed and improved for the excitation current with a pulse duration of 50 μs and a peak current of 4 kA, as was presented in Fig. 3.1.

3.2.1 Main Field Integral

The main field at the point of injection along the longitudinal z-axis is shown in blue in Fig. 3.3. The coordinate system is chosen such that the center of the magnet aligns with $z = 0$ mm, which implies that the copper box ends at $z = \pm$ 225 mm. The main field integral is calculated to be $Bdl_{main} = 257.34$ mTm, which corresponds to a magnetic length of $l_{eff} = 411.94$ mm for a deflection field of $B_0 = 624.8$ mT. The following analyses are therefore carried out for field values that lie above the nominal operation of the magnet. The values for the main field integral and the deflection field are linear with the current due to Ampere's law, which means that the current can be scaled to reach the desired deflection angle. Figure 3.3 also shows the approximation of the main field as a rectangle function with height B_0 and length l_{eff}.

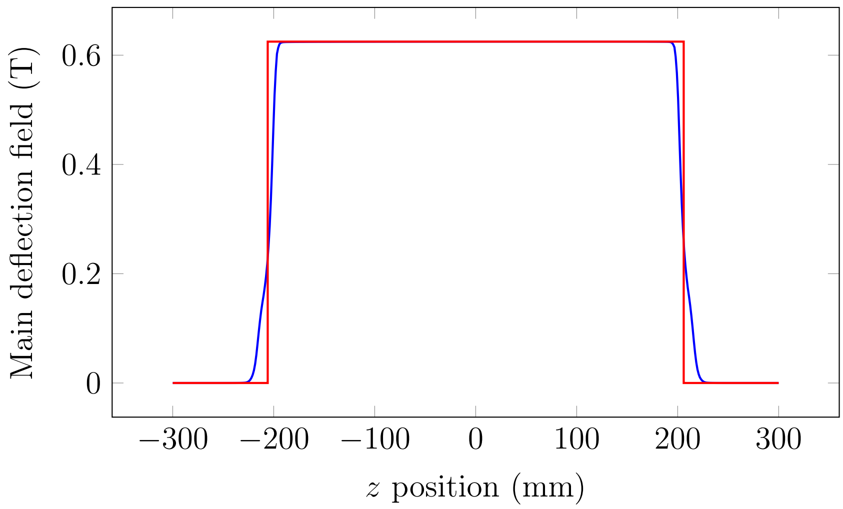

Fig. 3.3: Main deflection field at the point of injection (t = 12.5 μs) as a function of position (blue) and a simplification as a rectangle function with the same main field integral (red)

3.2.2 Main Field Homogeneity

Shims, otherwise known as poletips, can be added to optimize the homogeneity of the deflection field in the GFR (Eq. 3.1.1). This is shown in Fig. 3.4, where the poles are extended near the septum blade to decrease the distance between the magnetic north- and south pole, which in turn increases the magnetic field strength in this region [12]. The figure is not to scale as the the width w and the height h of the shim are on the micrometer scale and thus a lot smaller than the aperture height of 8 mm.

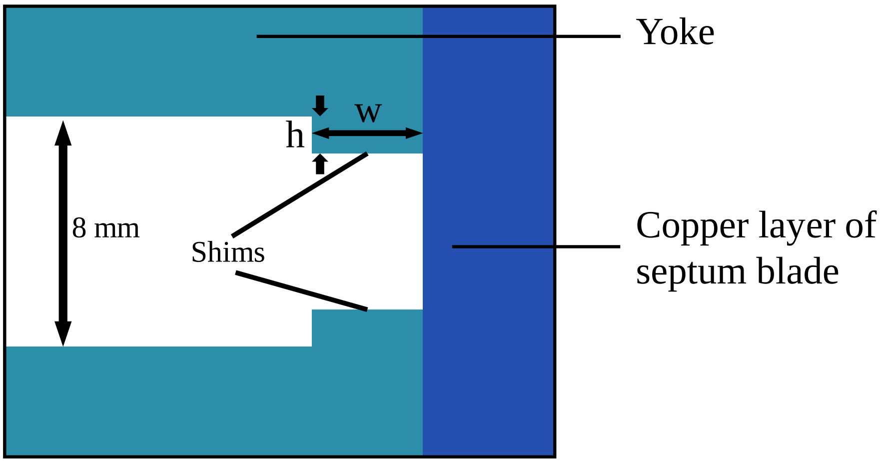

Fig. 3.4: Schematic overview of shims that improve the uniformity of the deflection field (not to scale)

The geometry of the shims is optimized with the goal to reduce $\mathcal{H}_1$ as much as possible, which then also reduces all higher magnetic field components C_n for n $\in \{1, 2, 3, \ldots\}$. The optimization is performed using two-dimensional simulations that are transient to account for the influence of the septum blade on the magnetic field in the GFR. The magnetic field is analyzed at the time of injection, which corresponds to t $= 12.5$ μs. The homogeneity without shims is shown in Fig. 3.5a. Here, the field decreases near the septum blade by a couple of milli-Tesla, resulting in a homogeneity of $\mathcal{H}_1 > 10^{-3}$. Figure 3.5b shows the homogeneity with an added shim on the side of the septum blade with a height $h = 70$ μm and a width $w = 240$ μm. The variations of the field go down by about one order of magnitude to about hundreds of micro-Tesla. A comparison of the uniformity of the field is shown in table 3.1, which shows that all metrics are improved by about one order of magnitude.

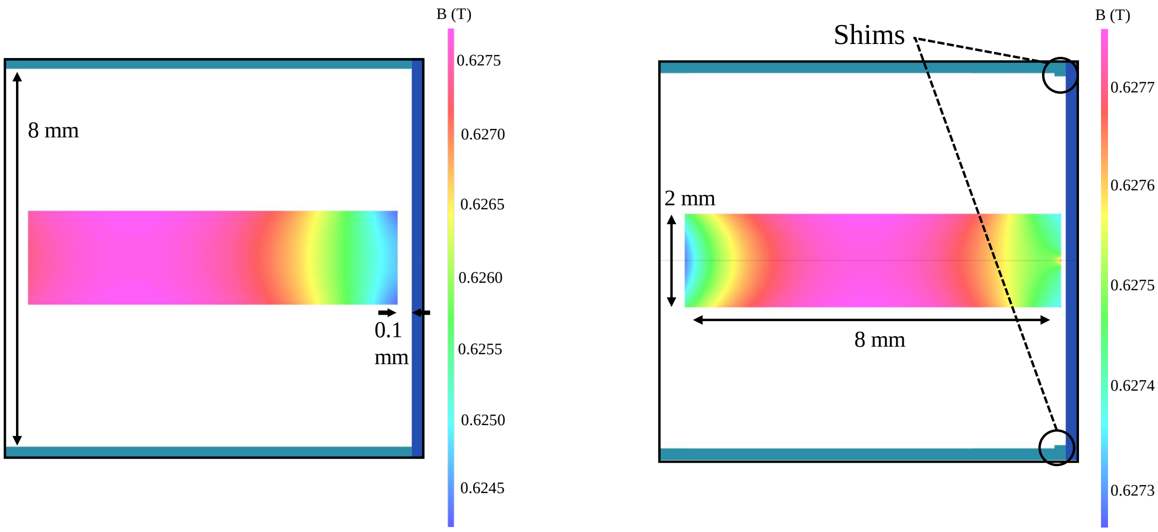

(a) Without Shims (b) With Shims

Fig. 3.5: Homogeneity of the magnetic deflection field in the GFR at the time of injection (t $= 12.5$ μs) with and without shims (the colors correspond to different values in both graphs)

Table 3.1: Achieved improvement of the uniformity of the magnetic deflection field by adding shims

	Dipole C_0 (mT)	Quadrupole C_1 ($\frac{mT}{mm}$)	Sextupole C_2 ($\frac{mT}{mm^2}$)	$\mathcal{H}_1$
No shims	627.020	5.051 $\cdot 10^{-1}$	-1.462 $\cdot 10^{-1}$	4.33 $\cdot 10^{-3}$
shims	627.732	1.005 $\cdot 10^{-2}$	-1.526 $\cdot 10^{-2}$	7.361 $\cdot 10^{-4}$

The optimized value of the geometry was obtained by iteratively checking different dimensions of the shim. The results of these simulations are shown as a three-dimensional plot in Fig. 3.6a and as a two-dimensional plot in Fig. 3.6b. These plots show that multiple combinations for h and w (colored in blue) lead to a similar improvement of the field uniformity of $\mathcal{H}_1 < 10^{-3}$. This set of geometries is shown in Fig. 3.7, where every pair of values (h, w) roughly has the same shim area of $A_{shim} \approx 0.016\ mm^2$.

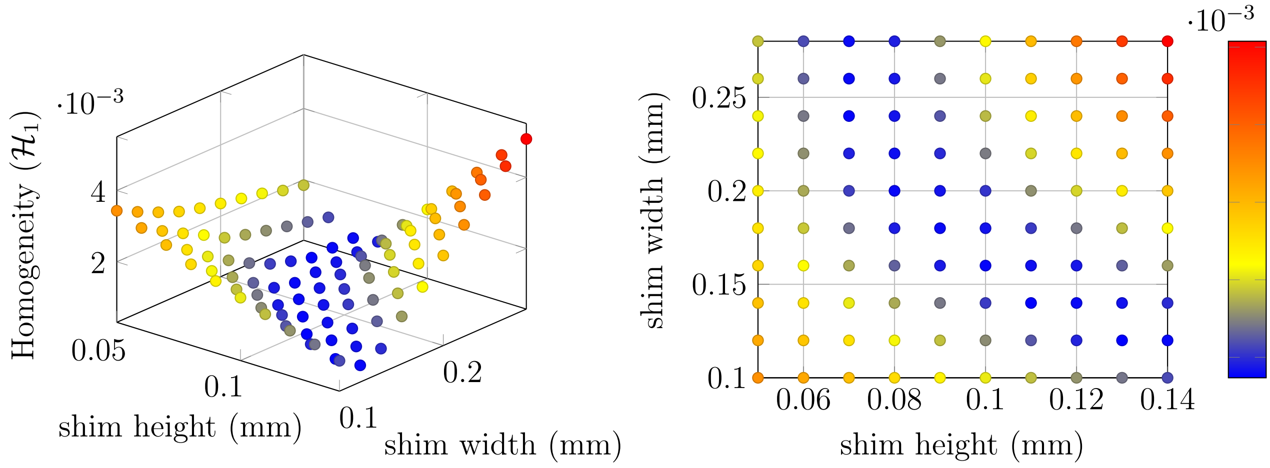

(a) 3D Plot

(b) 2D Plot

Fig. 3.6: Dependency of the homogeneity $\mathcal{H}_1$ of the magnetic deflection field on the width and height of the shim

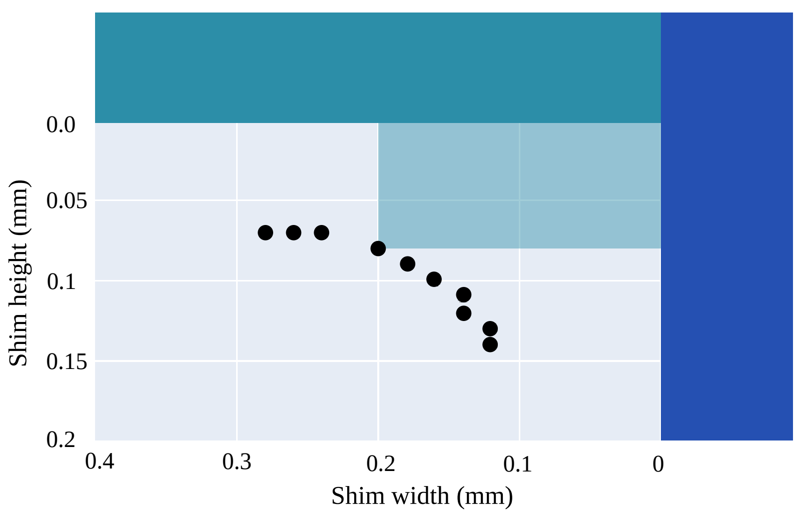

Fig. 3.7: Set of dimensions of the shim that improve the homogeneity of the main field to below 10^{-3}

3.3 Leakage Field

The basic shielding-principle of eddy-current septum magnets is, as said, the induction of eddy-currents in the septum blade. A basic approximation of the field-decay within a conducting material and the resulting shielding is given by the skin-effect:

$$\delta = \frac{1}{\sqrt{\mu_0 \mu_r \sigma f \pi}} \qquad \& \qquad B_{out} = B_{in} \cdot e^{\frac{-d}{\delta}} \tag{3.3.1}$$

This formula can be analytically derived for the harmonical case, meaning a stationary excitation with frequency f [6]. The actual excitation, however, is just a single sinusoidal pulse. Nevertheless, the formula still shows which physical quantities are important to reduce the leakage field and perturbations to the stored beam. In order to achieve minimal leakage field, the skin-depth δ should be a fraction of the septum thickness. This can be accomplished by increasing the **frequency** f, the **relative permeability** μ_r, the **conductivity** σ of the shielding material or of course by simply increasing the **septum blade thickness** d.

The **septum blade thickness** d was defined in the design specifications (Sec. 3.1) and it cannot be significantly increased, as the blade would be to close to the injected beam.

The **frequency** $f = \frac{1}{T}$ of the pulse is 20 kHz, which is fast compared to other eddy-current magnets, which are usually operated with a pulse duration T in the order of a few hundred microseconds. The frequency is chosen to be this high to induce more eddy-currents in the septum blade. A further increase of the frequency poses difficulties on the injection scheme, which will be explored in Sec. 3.3.6.

Both a high **conductivity** and a high **permeability** benefit the induction of eddy-currents, which motivates a two-layered septum blade where one material has a high conductivity and the other material has a high permeability. Copper is chosen as the first material, as its conductivity ($\sigma = 5.8 \cdot 10^7 \frac{S}{m}$) is the second highest conductivity of any material [13], except superconductors. The second layer is a ferro-magnetic material, as these usually have high permeabilities. A first option is a material called μ-metal, which is typically a composition of nickel, copper, iron and molybdenum. In the static case, μ-metal can achieve extremely high relative permeabilities of $\mu_r = 10^5$. There is, however, no available measurement for the permeability for a transient excitation with a 50 μs pulse. Measurements have only been performed for a frequency of up to 1 kHz, again in the harmonic case [14]. These measurements can be extrapolated to 20 kHz to obtain an approximation for the order of magnitude of the relative permeability μ_r of between 10^3 and 10^4. The saturation level of μ-metal is at around $B_{saturation} = 0.72$ T. Another option is ferromagnetic steel, which has a relative permeability in the following order of magnitude: $\mu_r = 10^2$ [7]. Table 3.2 gives an overview of the materials and their material properties for a frequency of f = 20 kHz.

Table 3.2: Properties of copper, ferromagnetic steel and μ-metal: Conductivity, permeability and skin-depth for a frequency f = 20 kHz

Material	σ ($\frac{S}{m}$)	μ_r	$B_{saturation}$ (T)	δ (μm)
Ferromagnetic Steel	$1.85 \cdot 10^6$	$\approx 10^2$	1.92	≈ 263
μ-metal	$1.67 \cdot 10^6$	$\approx 10^3 \dots 10^4$	0.72	$\approx 27.5 \dots 87.1$
Copper	$5.79 \cdot 10^7$	1	-	467

The table shows that ferromagnetic materials have smaller skin-depths and thus provide better shielding. However, saturation can start playing a role in ferromagnetic materials when the magnetic flux-density approaches the saturation level $B_{saturation}$. As a material saturates, its relative permeability decreases and therefore also its shielding quality, as can be seen in Fig. 2.3. This motivates the usage of copper as a first shielding-layer, because it drastically reduces the magnitude of the magnetic field before it enters the ferromagnetic second shielding-layer. This allows to operate the ferromagnetic material at a point with high permeability and good shielding properties.

3.3.1 Simulation Approach

Reducing Simulation Size & Simulation Time

As explained above in Sec. 3.3, the frequency of excitation of the SOLEIL EC septum magnet is quite high compared to previously designed and simulated ones. Therefore, the skin-depth especially in the ferromagnetic material becomes small and reaches in μ-metal only tens of micrometers. The simulation time of a full three-dimensional model can be approximated with a simulation runtime that scales as follows with the number of elements n in the mesh of the Finite Element Simulation: $t(n) = \mathcal{O}(n^{\frac{3}{2}})$ [15]. To model the skin-depth of a material, it is recommended by Opera® to have three elements for the first skin-depth, two elements for the second and one for the third (as shown in Fig. 3.8) [15]. The number of elements for just the first three skin-depths in the septum blade, with a length of 450 mm and a height of 13 mm, is hence about 500 million elements. This is calculated with a skin-depth of around 30 μm, a value which is possible for μ-metal as shown in Tab. 3.2. As a simulation with about 20 million elements takes about one day to run locally on one computer, the simulation runtime for a model with 500 million elements is $t_{sim} > 1 \text{ day} \cdot (\frac{500 \cdot 10^6}{20 \cdot 10^6})^{\frac{3}{2}} = 125$ days, making it unfeasible.

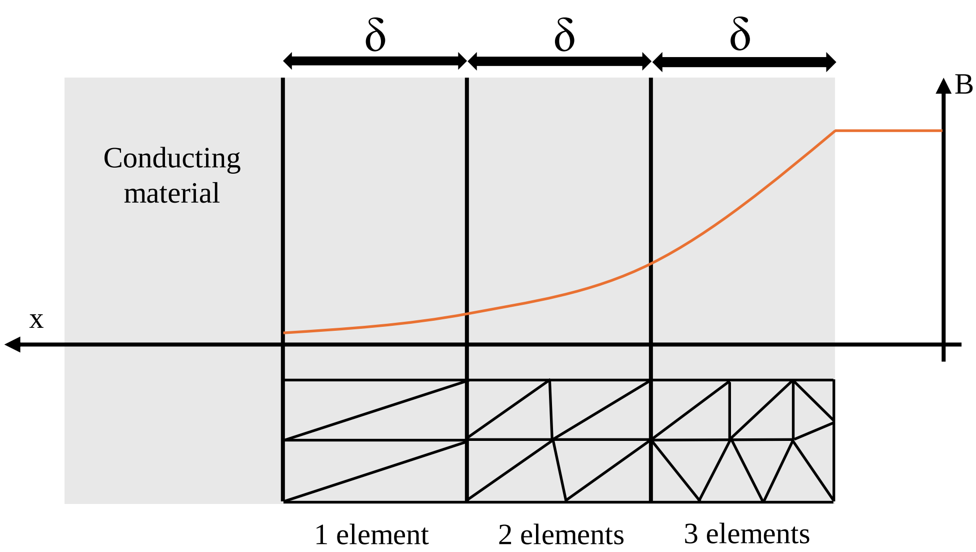

Fig. 3.8: **Necessary meshing to properly model the skin-effect**
The figure shows the decay of the magnetic field B in a conducting material in the first three skin-depth (δ) layers. It illustrates how this field-gradient must be meshed to guarantee accurate results.

In order to decrease this runtime while maintaining a good accuracy for the leakage field calculations, the entire magnet will be reconstructed using a set of two-and three-dimensional simulations. Figure 3.9 shows again the cross-section of the septum magnet in the xz-plane that is explained in detail in Fig. 2.2. It also includes a graph - $B_{leak}(z)$ - that outlines where significant amounts of leakage fields can be expected according to preliminary simulations and existing know-how regarding septum magnets [16]. First, stray fields can occur at both ends of the magnet right where the septum blade ends. These can be simulated using one three-dimensional simulation for each end. Secondly, residual fields can occur right behind the septum blade with an increasing magnitude as the septum thickness decreases. This is simulated with multiple two-dimensional simulations.

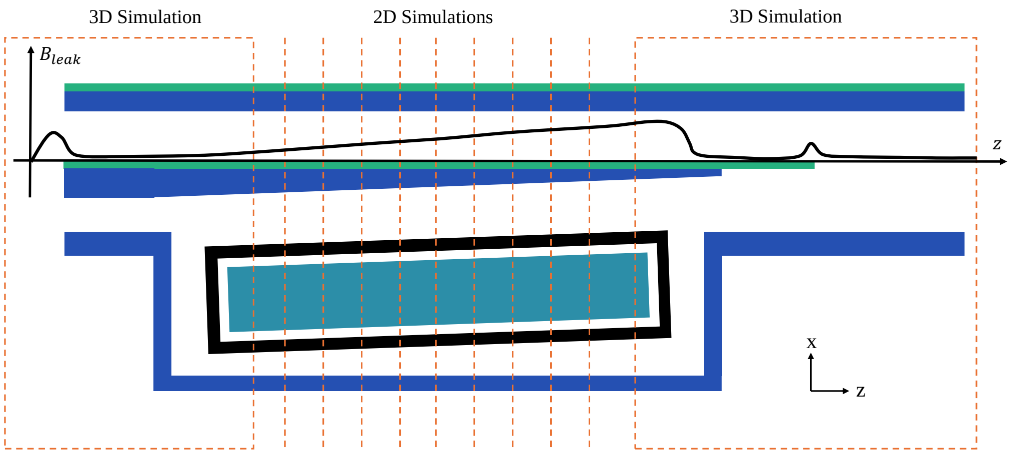

Fig. 3.9: **Sketch of the simulations approach**
The simulation is split up into three parts. The magnet's ends are simulated with three-dimensional simulations and the magnet's center is simulated with 26 two-dimensional simulations.

3.3.2 Copper Shielding and Validation of the Simulation Approach

To validate the simulation approach presented in Sec. 3.3.1, the magnet is first simulated without the additional shielding at both ends of the magnet and with a septum blade consisting only of one layer of copper (see Fig. 3.10). The model size is drastically reduced by these simplifications, allowing to simulate the entire model with one three-dimensional simulation, which can then be compared to a reconstruction using two- and three-dimensional simulations. Figure 3.10 also defines the z-axis to be the trajectory of the stored beam (e^-), which lies 5 mm away from the septum blade. The ends of the magnet are at z = ± 225 mm, giving the magnet a total length of 450 mm.

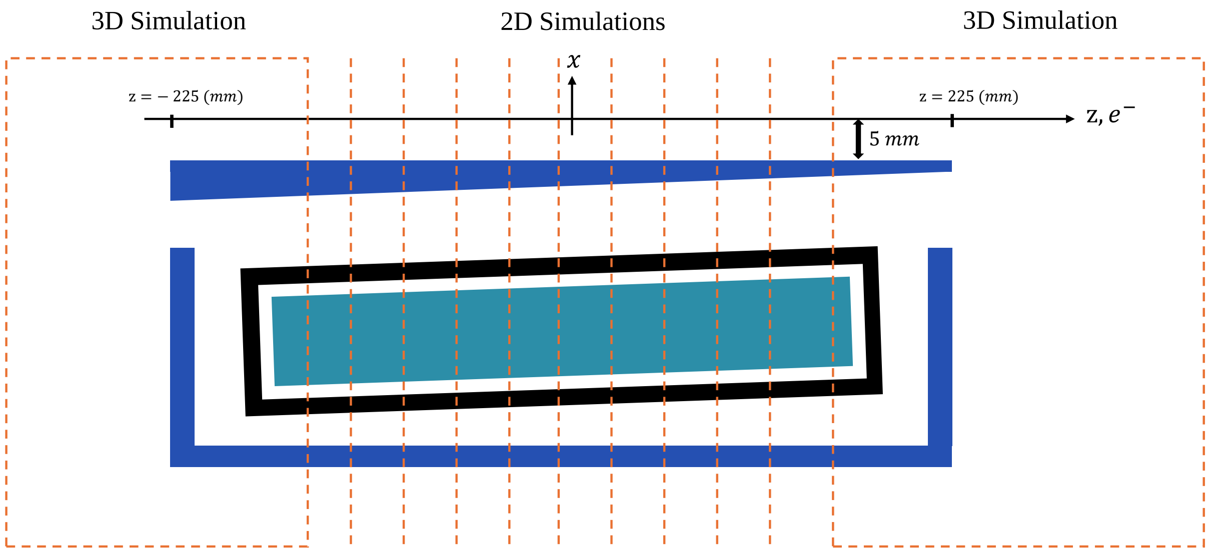

Fig. 3.10: Sketch of the simulation approach (as is also shown in Fig. 3.9) for a version of the septum magnet with only copper-shielding and simplified ends

3D Simulation

The result of the three-dimensional simulation can be seen in Fig. 3.11, which shows the magnetic field component B_y as a function of z-position and time. Both the components B_x and B_z can be neglected as they are practically zero due to the symmetry of the magnet. The highest magnitude for the stray field of around 9 mT appears at around $z = 200$ mm, which corresponds to the thin end of the septum with 0.5 mm of copper shielding. The stray fields decrease going towards the other end of the septum magnet because the septum thickness increases to 3 mm of copper shielding.

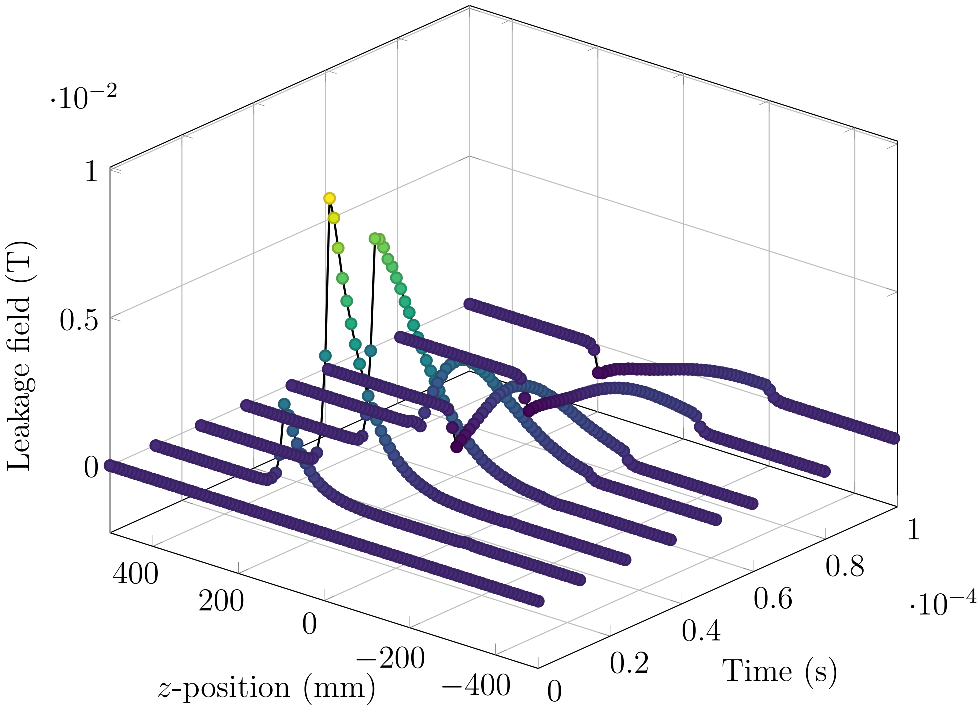

Fig. 3.11: **Transient three-dimensional simulation for a simplified version of the magnet**
The plot shows the magnetic leakage field at the position of the stored beam (z-axis) as a function of time.

Reconstruction

The three-dimensional simulation from the previous section will now be reconstructed using a set of two- and three-dimensional simulations as explained in Sec. 3.3.1. The extremities of the magnet are simulated using two three-dimensional simulations, one for the downstream side and one for the upstream side. The center of the magnet is simulated using 26 two-dimensional simulations, in which the septum thickness is increased by 0.1 mm with each simulation starting at 0.5 mm at the downstream end of the magnet.
A physically valid three-dimensional simulation for one of the magnet's extremities can be obtained by cutting the complete model into two parts at about 100 mm before the ends. Everything but the magnet's end is deleted from the model. The magnet is cut into two parts such that the cutting plane is perpendicular to the current carrying coil, it can thus be assumed that the magnetic field vectors are tangential to this cutting plane. Therefore, the boundary condition at the relevant faces is set to "tangential magnetic". An example of this is shown in App. A in Fig. A.3.
For two-dimensional simulations, an infinite length in the third dimension is assumed. The SOLEIL septum magnet is about three times as long as it is high and wide. Furthermore, the magnet has a changing cross-section because of the increasing septum blade thickness. However, the angle at which the thickness increases is small with $\alpha = arctan(\frac{2.5}{450}) = 0.318°$. This means that the rate of change of the cross-section is also small, making two-dimensional simulations a valid approximation for the magnet's center.
The result of the three-dimensional and two-dimensional simulations are shown in Fig. 3.12 and Fig. 3.13 respectively.

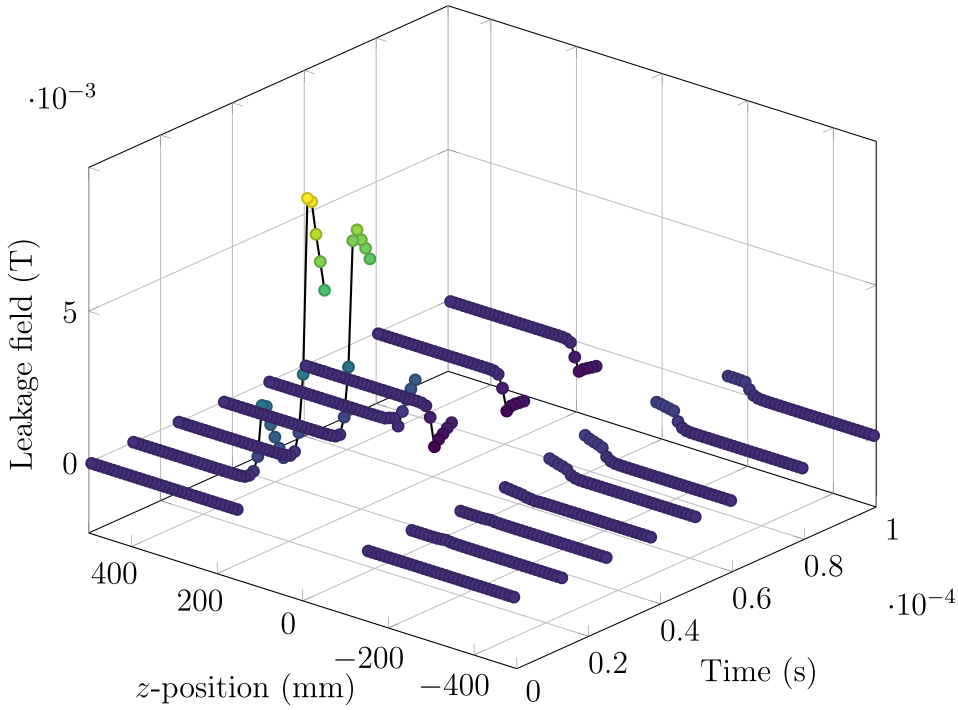

Fig. 3.12: **Transient three-dimensional simulation of the magnet's ends for a simplified version of the magnet**
The plot shows the magnetic leakage field at the position of the stored beam (z-axis) as a function of time for both ends.

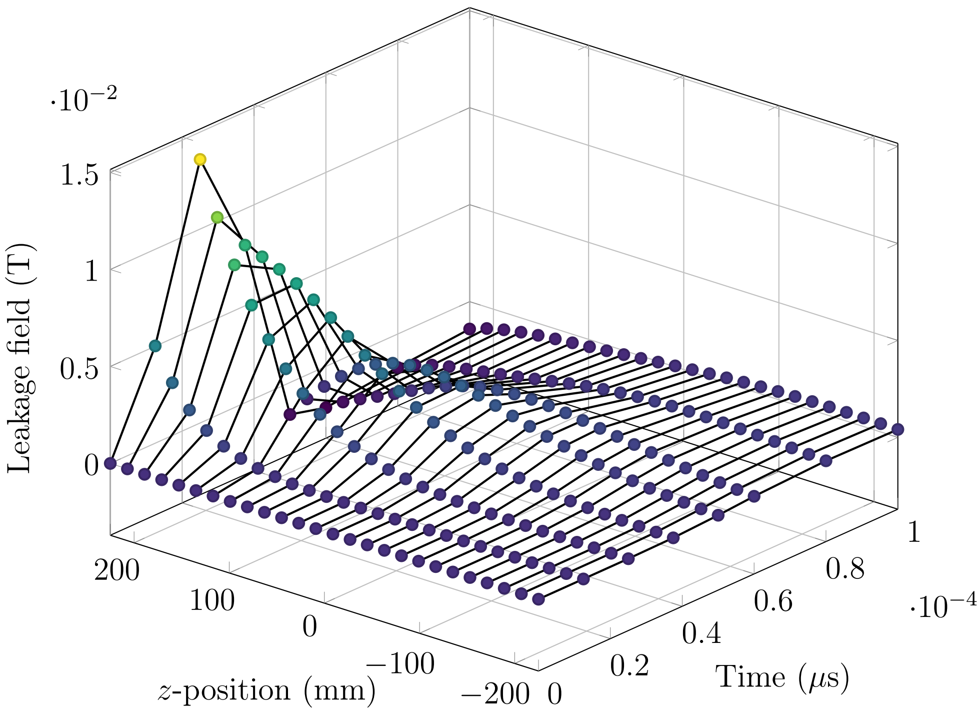

Fig. 3.13: **26 Transient two-dimensional simulations of the magnet's center for a simplified version of the magnet**
The plot shows the magnetic leakage field at the position of the stored beam (z-axis) as a function of time for the central part of the magnet.

The simulated data shown in Fig. 3.12 and Fig. 3.13 can now be combined to obtain a full description of the magnetic stray field. For this, the data points from the two-dimensional simulations are inserted in between the two three-dimensional simulations, the result of which is shown in Fig. 3.14.

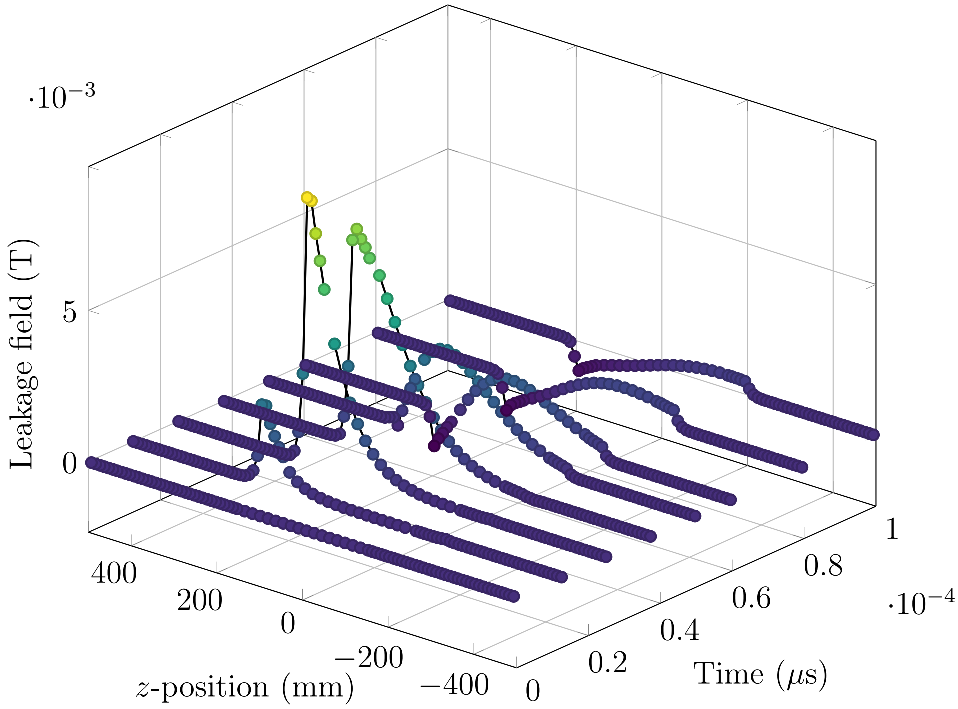

Fig. 3.14: **Reconstructed magnetic leakage field for a simplified version of the magnet**
The simulations from Fig. 3.11 and 3.13 are combined to reconstruct the leakage field of the complete model.

Comparison

The result from the reconstruction (see Fig. 3.14) is now compared to the result that was obtained using only one three-dimensional simulation (see Fig. 3.11). To reduce the number of data points that need to be compared, Eq. 2.4.2 will be used to calculate the leakage field integral $Bdl_{leakage}$ as a function of time. This corresponds to taking the area (after taking the absolute value of B_y) of each curve in Fig. 3.14 and 3.11, with one curve corresponding to one time-step. The leakage field integrals from the reconstruction and the full three-dimensional model are shown in Fig. 3.15. It can be seen that the reconstruction yields the same result, while it drastically reduces the model size and simulation runtime.

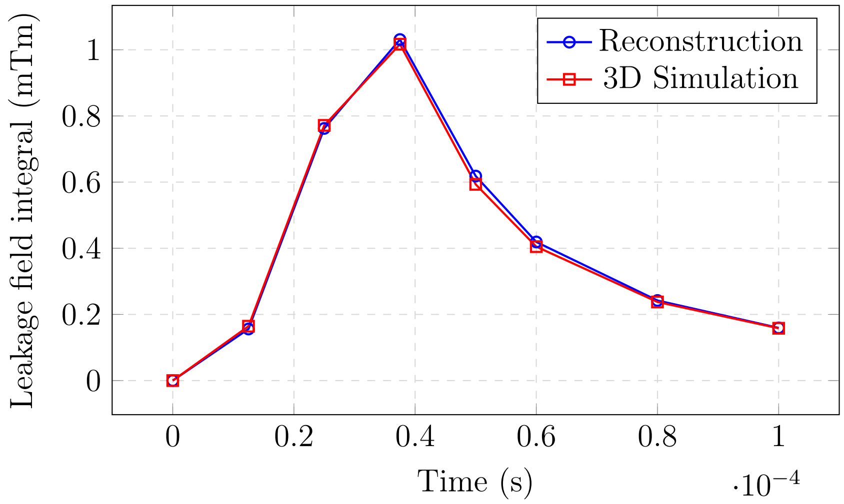

Fig. 3.15: Comparison of the leakage field integral of a simplified magnet between the reconstruction comprising two-dimensional and three-dimensional simulations and a complete three-dimensional simulation

Furthermore, the plot shows that the leakage field integral reaches values of up to 1 mTm, which is significantly higher than the specified value in Sec. 3.1 of $Bdl_{leakage} < 10\ \mu$Tm, which ensures a limitation of the perturbations of the stored beam. It is therefore not sufficient to rely solely on copper shielding, which necessitates the analysis of a two-layer septum blade that also includes an additional layer of ferromagnetic material.

3.3.3 μ-Metal and Copper Shielding

The full model of the septum magnet, as it was shown in Fig. 2.2, will now be analyzed with μ-metal as the ferromagnetic second layer of the septum blade. As discussed in Sec. 3.3, μ-metal can significantly reduce the magnetic stray field due to skin-depths that are in the order of only tens of micro-meters. However, this drastically increases the model size and leads to simulation run-times that are impractical, which is why the reconstruction method of the previous section is used.

BH-Curve

μ-metal is a nonlinear material, meaning that the permeability μ is not a constant and instead depends on the magnetic field-strength H and the flux-density B. To account for this non-linearity, the BH-characteristic of μ-metal needs to be fed into the simulation software Opera®. This BH-curve is usually obtained through measurement. For μ-metal, however, measurements are only available for frequencies of up to 1 kHz, whereas the frequency of excitation for the SOLEIL septum magnet is 20 kHz. To still approximate the effect of non-linearity and saturation, the BH-characteristic is generated manually for different initial permeabilities μ_r^{init}. Furthermore, Opera® imposes certain constraints on the BH-curve that improve the convergence properties of non-linear simulations. Accordingly, the following constraints are defined for the BH-characteristic:

1. initial relative permeability $\mu_r^{init} = \frac{1}{\mu_0}\frac{dB}{dH}|_{H=0}$
2. Saturation level $B_{sat} = lim_{H\to\infty}$ B(H) - $\mu_0 \cdot H$
3. $B(H)$ must be differentiable and continuous

4. $\mu(H)$ must be a monotonically decreasing function (improves convergence)

5. $\frac{d\mu}{dH}$ must be a monotonically increasing function (improves convergence)

These constraints limit the number of possible BH-curves for a given initial relative permeability and saturation level. Figure 3.16a and Fig. 3.16b show the resulting BH-characteristics for an initial relative permeability of $\mu_r^{init} = 10^3$ and $\mu_r^{init} = 10^4$ respectively.

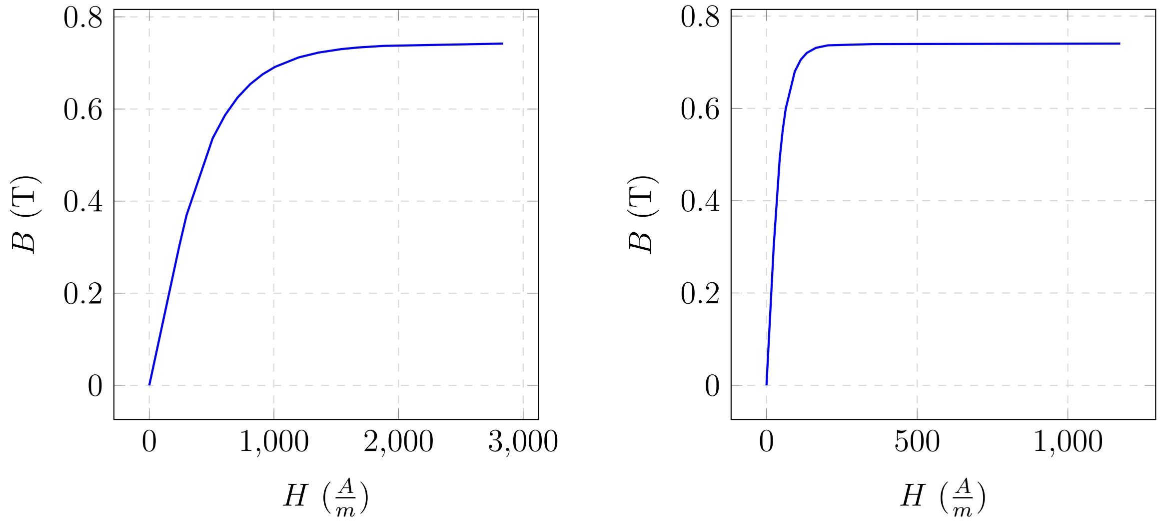

(a) $\mu_r^{init} = 10^3$ and $B_{sat} = 0.72$ T

(b) $\mu_r^{init} = 10^4$ and $B_{sat} = 0.72$ T

Fig. 3.16: Manually generated BH-curves for μ-metal at different initial permeabilities μ_r^{init}

Reconstruction

To reconstruct the full magnet, it will be split up into two three-dimensional simulations and 26 two-dimensional simulations, as was previously shown in Fig. 3.9. The three-dimensional simulations capture all stray-fields at the magnet's ends, while the two-dimensional simulations capture all residual fields that pass through the septum blade.
The reconstruction of the magnetic stray-field is obtained in the same way as in Sec. 3.3.2, the resulting plot for $\mu_r^{init} = 10^3$ (BH-curve in Fig. 3.16a) is shown in Fig. 3.17. It can be seen that the stray fields resulting from end-effects are significantly smaller than the magnetic residual fields that pass through the septum blade. This is because no additional peaks are present at $z > 225$ mm or $z <$ -225 mm. The leakage field integral $Bdl_{leakage}$ is consequently dominated by the magnet's center, which motivates using only two-dimensional simulations as end-effects are negligible.

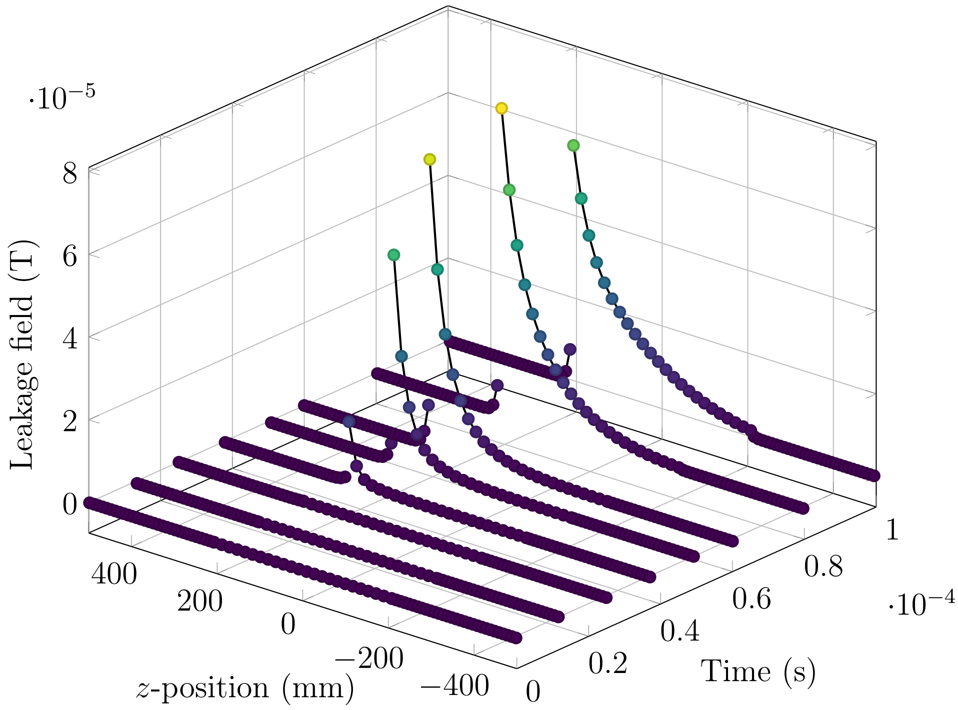

Fig. 3.17: **Reconstructed magnetic leakage field for a two-layer septum blade comprising copper and μ-metal with a permeability of μ-metal of $\mu_r^{init} = 10^3$**
The plot shows the magnetic leakage field at the position of the stored beam (z-axis) as a function of time.

The leakage field integral as a function of time (Eq. 2.4.2) is shown in Fig. 3.18a, once for a reconstruction composed of three-and two-dimensional simulations and for a reconstruction using only two-dimensional simulations. The first simulation shows a peak value for the leakage field integral of 6.3 μTm, whereas the latter shows a peak value of 7.3 μTm. The difference is caused by the assumption that the field abruptly drops to zero at z = ± 225 mm for a reconstruction using only two-dimensional slices. In reality, the leakage field starts to decay before z = ± 225 mm, which is modeled more accurately by the three-dimensional simulations.
The result for $\mu_r^{init} = 10^4$ is obtained using only two-dimensional simulations, the result is shown in Fig. 3.18b. The peak value of the leakage field integral drops by about one order of magnitude from 7.3 μTm to about 0.35 μTm as the permeability is increased by one order of magnitude from $\mu_r^{init} = 10^3$ to 10^4. Moreover, this peak value occurs after around 450 μs for $\mu_r^{init} = 10^4$, compared to 90 μs for $\mu_r^{init} = 10^3$. This means that a higher permeability of the ferromagnetic material leads to a smaller leakage field, but it also causes a longer propagation time of the the magnetic field through the septum blade.

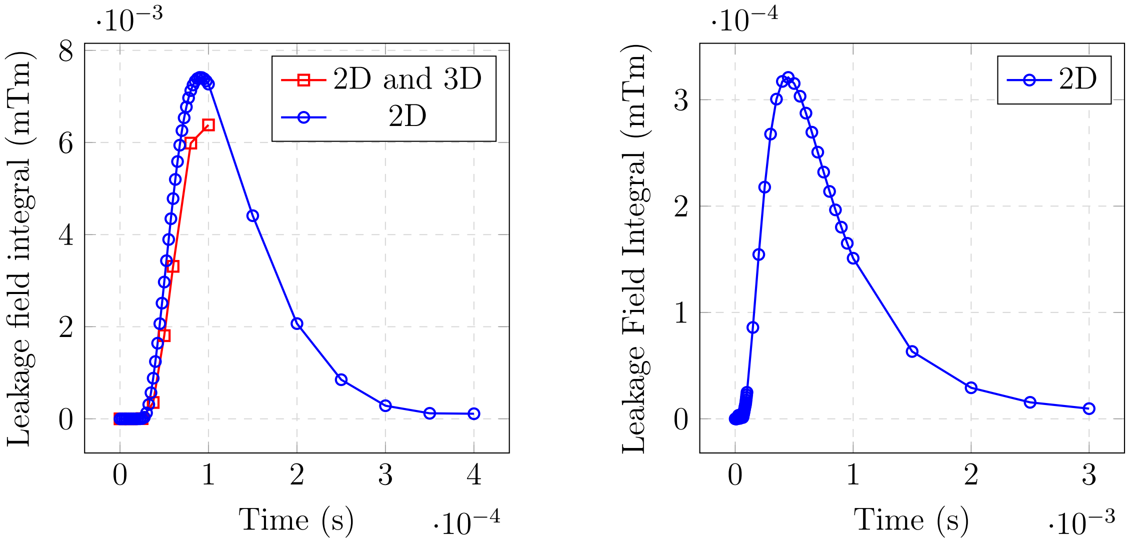

(a) $\mu_r^{init} = 10^3$ (b) $\mu_r^{init} = 10^4$

Fig. 3.18: **Leakage field integral for a two-layer septum blade comprising copper and μ-metal**
The plot shows the leakage field integral as a function of time for two different BH-curves of μ-metal. Each dot corresponds to the value of one simulated time-step. These are connected linearly.

The integrated quadrupole component can be obtained similarly to the integrated dipole component. For each position z, the quadrupole component can be calculated using Eq. 2.3.3. It is calculated at a distance d = 5 mm from the septum blade, all of these values for different z-values are then integrated to get the integrated quadrupole component seen by the particle beam. The result of this is shown in Fig. 3.19a for $\mu_r^{init} = 10^3$ and in Fig. 3.19b for $\mu_r^{init} = 10^4$. The corresponding peak values of the integrated quadrupole are $Bdl_{leak,QP} = 1.52 \cdot 10^{-3} \frac{T}{m} m$ and $Bdl_{leak,QP} = 6.24 \cdot 10^{-5} \frac{T}{m} m$ respectively, which lie below the specified value of Sec. 3.1 of $0.02 \frac{T}{m} m$. The shielding therefore ensures that the stored beam stays concentrated due to a sufficiently low quadrupole field, as the presence of this magnetic harmonic causes a defocusing of the beam as was explained in Sec. 2.5.

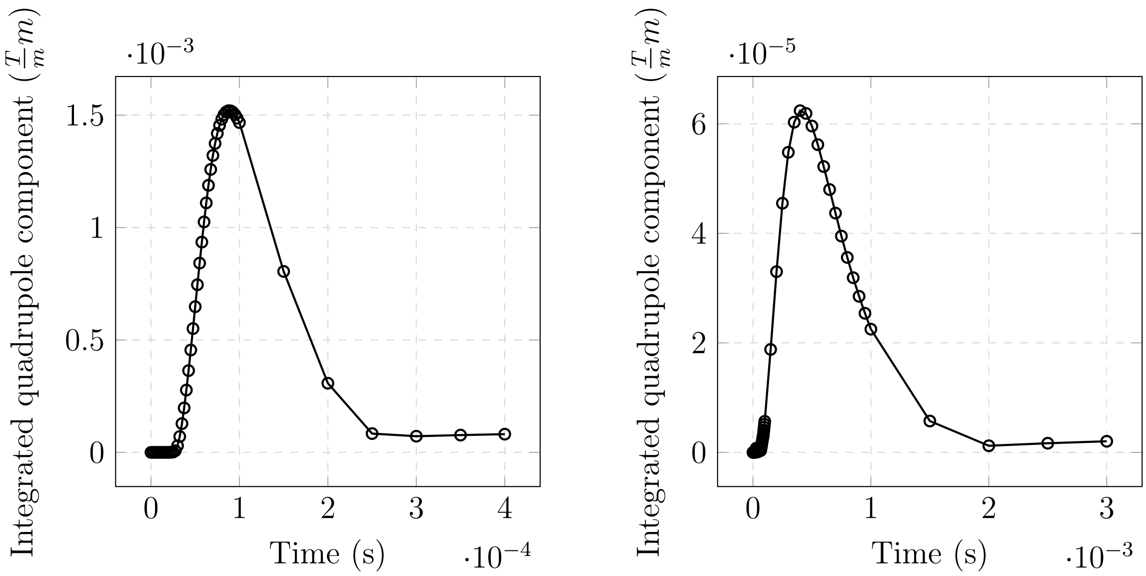

(a) $\mu_r^{init} = 10^3$ (b) $\mu_r^{init} = 10^4$

Fig. 3.19: **Integrated quadrupole component for a two-layer septum blade comprising copper and μ-metal**
The plot shows the integrated quadrupole component as a function of time for two different BH-curves of μ-metal. Each dot corresponds to the value of one simulated time-step. These are connected linearly.

Dependency on permeability

In the previous section, the leakage field was calculated for the two relative permeabilities $\mu_r^{init} = 10^3$ and 10^4. A more comprehensive understanding of the dependency of the leakage field on the permeability can be achieved by getting more data-points for different permeabilities. Therefore, the maximum leakage field is simulated **linearly** (as opposed to all previous simulations that were nonlinear) for the two-dimensional cross-section of the SOLEIL II septum magnet (see Fig. 2.1) for relative permeabilities of μ-metal that range from 10^2 to 10^5. The result of the simulation can be seen in blue in Fig. 3.20, once for a copper-thickness in the septum of 0.5 mm and once with 3 mm. Both curves are parallel, which confirms that the dependency of the shielding quality on the permeability does not depend on the magnitude of the magnetic field - which is to be expected for linear simulations.
Both plots show that the leakage field drops by about one order of magnitude for every increase in the order of magnitude of the permeability. A more precise correlation between the leakage field and the permeability can be found by fitting the simulated data to the function $f(x) = a \cdot x^b$ using the least-squares method. The results are plotted in red in Fig. 3.20, showing that the dependency is roughly as follows: $B_{leak}^{max} \propto \frac{1}{\mu^{1.1}}$.

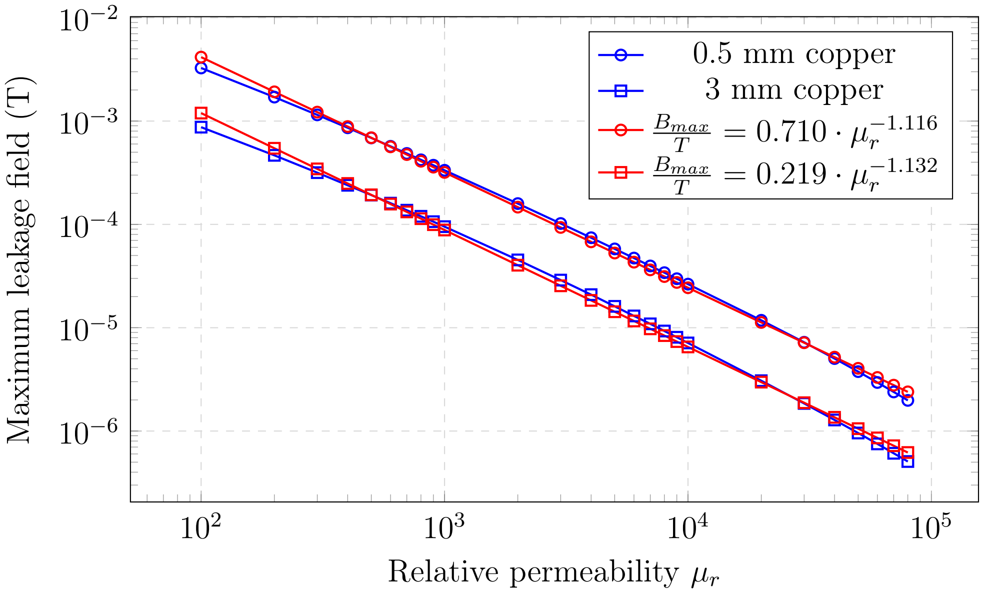

Fig. 3.20: **Dependency of the leakage field on the relative permeability**
The maximum value of the leakage field is plotted as a function of the permeability of μ-metal for two different thicknesses of copper in the septum blade.

This relation between the punctual leakage field value and the permeability can be extended mathematically to the leakage field integral. From Fig. 3.20, the relation $B_{leak}^{max}(z,\mu) \propto \frac{1}{\mu^{1.1}}$ was concluded. This implies that the same relation holds for the integrated leakage field: $Bdl_{leak} \propto \frac{1}{\mu^{1.1}}$. This can be seen using the following steps:

$$Bdl_{leak}^{max} = \int B_{leak}^{max}(z)dz$$

With $B_{leak}^{max}(z) = \frac{1}{\mu^{1.1}} \cdot const(z)$, we conclude that

$$Bdl_{leak}^{max} = \frac{1}{\mu^{1.1}} \cdot \int const(z)dz \propto \frac{1}{\mu^{1.1}}$$

Hence, the dependency that holds for punctual leakage field values also holds for the leakage field integral. This corresponds well with the simulated leakage field integrals that were obtained in the previous section. The maximum leakage field integral drops by about one order of magnitude from $7{\cdot}10^{-3}$ to $3.5{\cdot}10^{-4}$ as the permeability is increased by one order of magnitude (see Fig. 3.18).

3.3.4 Steel and Copper Shielding

For the last configuration of the septum magnet that was shown in Fig. 2.2 ferromagnetic steel will be used as the second layer of the septum blade. The septum blade therefore comprises a 0.5 mm blade of ferromagnetic steel and, as before, a tapered layer of copper that decreases in thickness from 3 mm to 0.5 mm.

BH-curve

As with μ-metal, there is no measured BH-curve for a frequency of 20 kHz, so a BH-curve is again manually generated as was shown in Sec. 3.3.3. The BH-curve has an initial relative permeability of $\mu_r^{init} = 10^2$ and is shown in Fig. 3.21.

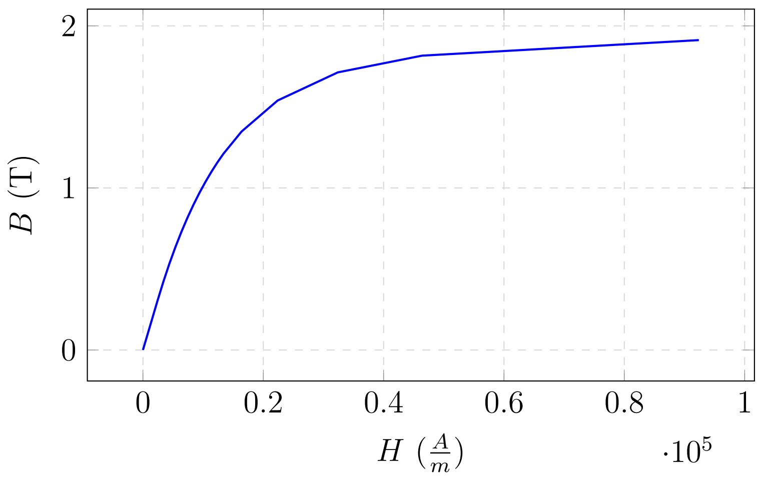

Fig. 3.21: Manually generated BH-curve for steel with $\mu_r^{init} = 10^2$ and $B_{sat} = 1.92$ T

Reconstruction

The reconstruction of both the integrated dipole component and the integrated quadrupole component is obtained as before, the results are shown in Fig. 3.22a and 3.22b respectively. Both integrated field components exceed the values that were specified in Sec. 3.1. The integrated dipole component goes up to more than 0.1 mTm, which is about one order of magnitude higher than the acceptable value of the leakage field integral of $Bdl_{leak} < 10$ μTm. Therefore, it can be concluded that ferromagnetic steel does not provide sufficient shielding.

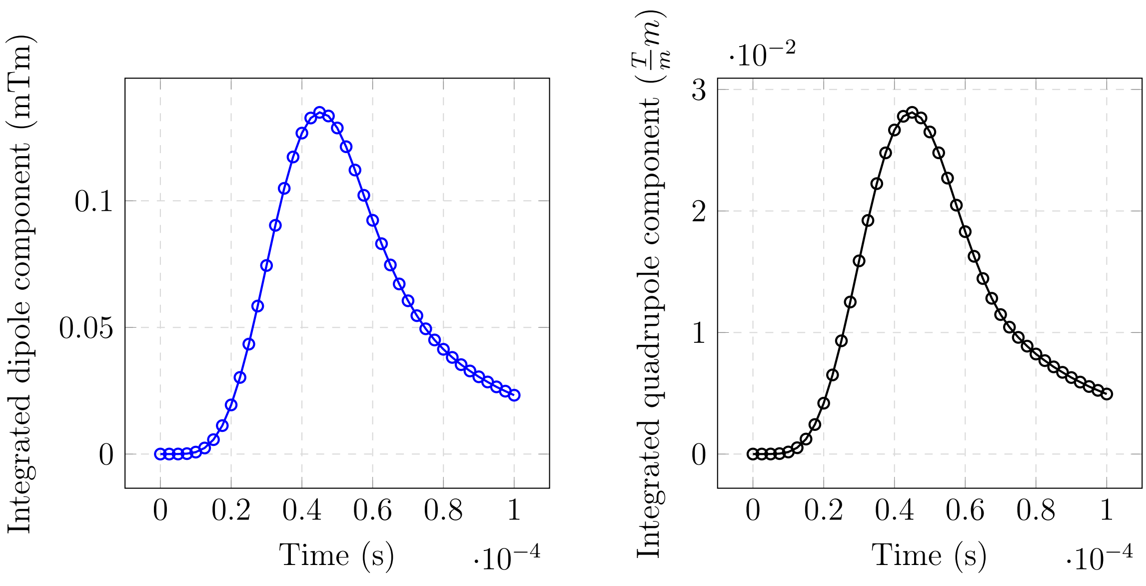

(a) Dipole

(b) Quadrupole

Fig. 3.22: Integrated dipole and quadrupole fields for a composite septum blade comprising copper and ferromagnetic steel at a permeability of $\mu_r^{init} = 10^2$

3.3.5 Comparison

Table 3.3 summarizes the results that were acquired in this chapter. It can be seen that firstly, copper shielding does not suffice because the specified value for the leakage field integral of $Bdl_{leakage} < 10$ μT is exceeded by about two orders of magnitude. Secondly, a two-layer shielding constituting ferromagnetic steel and copper does not suffice either, as the specified value for the leakage field integral is exceeded by one order of magnitude. For μ-metal, the calculated values for both the integrated dipole and quadrupole field lie within the specified range. The shielding performance of μ-metal increases by one order of magnitude as the permeability increases by one order of magnitude (shown in Sec. 3.3.3). The actual shielding performance of the magnet, however, can only be determined using measurements as the simulations rely on assumptions, especially with respect to the material properties of μ-metal.

Table 3.3: Comparison of the integrated dipole field (Bdl_{DP}) and the integrated quadrupole field (Bdl_{QP}) for different septum blade materials and different material properties

		$\mu_r = 10^0$	$\mu_r^{init} = 10^2$	$\mu_r^{init} = 10^3$	$\mu_r^{init} = 10^4$
Copper	Bdl_{DP} (mTm)	1.02	no ferromagnetic material		
	Bdl_{QP} ($\frac{T}{m}m$)	-			
Steel & Copper	Bdl_{DP} (mTm)	-	$1.35 \cdot 10^{-1}$	$\mu_r^{init} < 10^3$	
	Bdl_{QP} ($\frac{T}{m}m$)		$2.81 \cdot 10^{-2}$		
μ-Metal & Copper	Bdl_{DP} (mTm)	$\mu_r^{init} > 10^2$		$7.41 \cdot 10^{-3}$	$3.21 \cdot 10^{-4}$
	Bdl_{QP} ($\frac{T}{m}m$)			$1.52 \cdot 10^{-3}$	$6.24 \cdot 10^{-5}$

3.3.6 Outlook - Faster pulsing

The influence of the pulsing frequency on the leakage field is explored in this section. A higher frequency - or a shorter pulse - generates more eddy-currents which consequently improves the shielding. However, a faster pulse also makes injection more difficult as it results in a notable kick error, which refers to different parts of the injected beam being subject to a different magnetic field. This is elaborated on in Fig. 3.23, which shows how the particle bunch in the SOLEIL accelerator with a length of 304 ns traverses through the magnetic field. The resulting kick error at nominal deflection field for a pulse width of 10 μs can be calculated using Eq. 2.4.1 : $\theta_{error} = 90$ μrad. This can be compensated by adding a third harmonic to the excitation pulse to flatten the top of the deflection field [5]. Regardless, faster pulsing is only briefly inspected in this section as it introduces new problems.

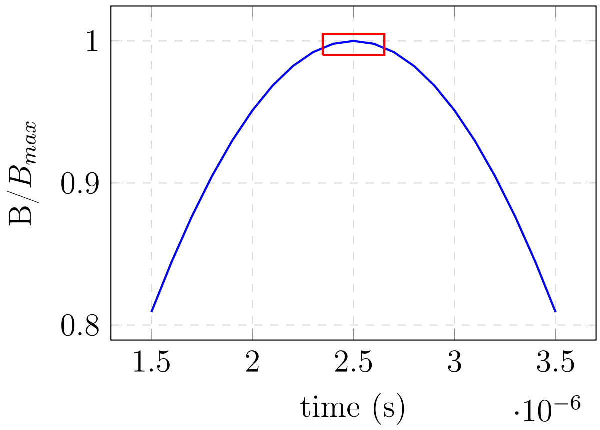

Fig. 3.23: **Kick error for a pulse width of 10 μs**
The blue curve shows the deflection field as a function of time. The injected bunch with a length of 304 ns (indicated in red) is subject to different magnetic field strengths, causing a kick error.

Fig. 3.24 shows the leakage field as a function of time for pulse widths going from 50 μs - the frequency of all previous simulations - down to 10 μs. The plot shows how the leakage field decreases as the frequency is increased. Fig. 3.25 is then obtained by plotting the maximum values of the leakage field for different excitation frequencies. The red curve fits the simulated data points to the function $f(x) = a \cdot x^b$ using the least-squares method, which shows the following dependency: $B_{leak}^{max} \propto \frac{1}{f^{1.58}}$. This means that an increase of frequency from f = 20 kHz (T = 50 μs) to f = 100 kHz (T = 10 μs) would lower the leakage field by about one order of magnitude: $\frac{B_{leak}(f=20kHz)}{B_{leak}(f=100kHz)} = \frac{100}{20}^{1.58} = 11.18$. A 30 μs pulse can be a compromise as the leakage field is reduced by a factor of two while the kick error remains at a reasonable value of 10 μrad.

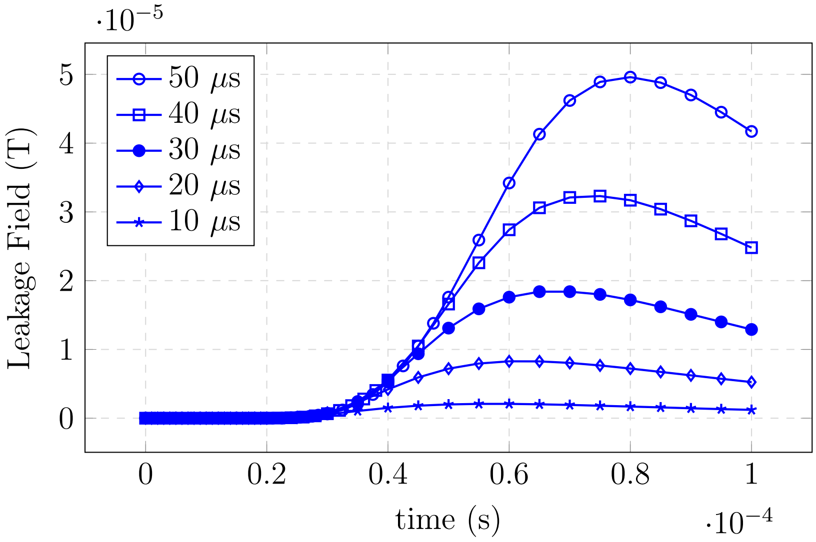

Fig. 3.24: **Leakage field for different excitation frequencies**
The plot shows the leakage field as a function of time five millimeters away from a two-layer septum blade comprising μ-metal and copper for different excitation frequencies.

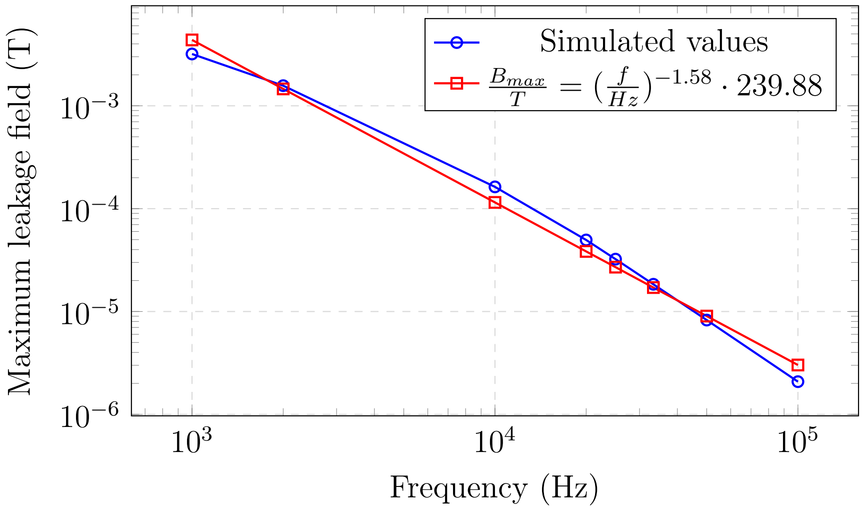

Fig. 3.25: **Dependency of the leakage field on the excitation frequency**
The plot shows the simulated maximum leakage field as a function of the excitation frequency (blue) and a curve that fits the data (red).

3.4 Simulations - Discussion

In this chapter, a comprehensive magnetic analysis of the SOLEIL II eddy-current injection septum magnet was performed with respect to the main deflection field and the leakage field.
An improvement of the uniformity of the main deflection field of about $8 \cdot 10^{-4}$ was achieved in Sec. 3.2.2 by adding shims to the poles of the magnet. This homogeneity ensures that the main field is predominantly comprised of the dipole harmonic, while all higher field harmonics are reduced because they cause unwanted perturbations to the injected beam. However, the actual uniformity will be limited by the mechanical precision of the assembly of the yoke since the dimensions of the shim are in the order of hundreds of micro-meters.
Next, an analysis of the leakage field was carried out in Sec. 3.3 for three different septum blades. First, a simulation approach was established and verified that reduces both the simulation size and the runtime, making the simulation of large models with small skin-depths feasible. This was achieved by reconstructing the complete model with a set of two- and three-dimensional simulations. Using this simulation strategy, it was shown that a two-layered septum blade comprising a tapered blade of copper and a 0.5 mm blade of μ-metal meets the strict requirements of the leakage field of $Bdl_{leakage} < 10$ μTm. The simulations were carried out with a current of 4 kA that generates a main field of $Bdl_{main} = 257.34$ mTm, resulting in a ratio $\frac{Bdl_{leak}}{Bdl_{main}} < 4 \cdot 10^{-5}$.
However, this analysis heavily relied on assumptions about the permeability and BH-characteristic of μ-metal, as no measurements have been performed for the given excitation frequency of 20 kHz. Measurements will have to confirm the material properties of μ-metal and its permeability. The simulations of this chapter can then be used to more precisely estimate the leakage field integral by using the results of section 3.3.3. It was shown that the leakage field scales with the permeability as follows: $Bdl_{leak} \propto \frac{1}{\mu_r^{1.1}}$. Lastly, the possibility of even faster pulsing has been discussed in Sec. 3.3.6 to further reduce the leakage field. A pulse width of 30 μs has been shown to reduce the leakage field by a factor of two while not causing a substantial kick error.

4 Benchmarking

This chapter aims to benchmark the simulations by comparing their results with magnetic measurements that were carried out for two other septum magnets. The first magnet is the CERN SMH16-CF (Septum Magnet Horizontal 16 - Courant Foucault), installed in the straight section 16 of the CERN Proton Synchrotron (PS) accelerator, and will be used for beam extraction in the CERN particle accelerator complex. It will replace the current SMH16 which extracts protons and ions from the PS into the TT2 transfer line and towards the experimental areas of the PS and the Super Proton Synchrotron (SPS) [17]. The CERN accelerator complex can found in App. A in Fig. A.9.
The second magnet is the spare version of the SOLEIL eddy-current septum magnet that is currently used for beam injection in the SOLEIL accelerator. The measurements for SMH16-CF and for the SOLEIL spare septum magnet are presented in Sec. 4.1 and 4.2 respectively. The measurements are compared to simulations that are obtained in the same way as was shown in the previous chapter. This is followed in Sec. 4.3 by a discussion of the results.

4.1 SMH16-CF Measurement

The SMH16-CF will be measured using a power converter that provides a half sine pulse with a pulse width of around 640 μs. This, however, is not the designated power converter that will be used in the magnet's final configuration. The dedicated pulse generator produces a 400 μs full sine pulse with an added third harmonic, which flattens the top of the pulse in order to reduce the kick error that was explained in Sec. 3.3.6. A full sine excitation is used as it has been shown to result in lower leakage field values and also smaller time constants, which determine the rate of decay of the stray fields [18].
The current of the power converter is measured using a Rogowski-coil and this measurement is then used as an input for the simulation. The magnetic measurement is carried out using a punctual magnetic probe, which is a copper wire with a certain number of windings and a well known effective area. A voltage is induced in this copper wire by the induction law (Eq. 2.2.1) as all magnetic fields are time-varying: $U_{ind} = A_{eff} \cdot \frac{dB}{dt}$. The magnetic field is obtained by integrating the measured voltage over time and dividing by the effective area:

$$B(t) = \frac{1}{A_{eff}} \int_{t_{start}}^{t} U_{ind}(\tilde{t}) d\tilde{t} \tag{4.1.1}$$

The effective area for this probe is $A_{eff} = 0.03693\ mm^2$. A large effective area increases the signal and should facilitate the measurements of leakage fields that are in the milli-Tesla range. The probe was calibrated by the magnetic measurement group of CERN.
Figure 4.1 shows the horizontal cross-section of SMH16-CF. For this magnet, the septum blade is one layer of either copper or aluminum with a thickness of 3 mm along the entire longitudinal axis. Copper has better shielding qualities as its conductivity ($\sigma = 5.8 \cdot 10^7 \frac{S}{m}$) is higher than the conductivity of aluminum ($\sigma = 3.53 \cdot 10^7 \frac{S}{m}$) [13] . However, aluminum

is of interest because of its radiation absorption properties [19]. Furthermore, the magnet has a total length of 1125 mm with a symmetry axis at the center of the magnet along the longitudinal axis. Consequently, only half of the magnet is measured and simulated.

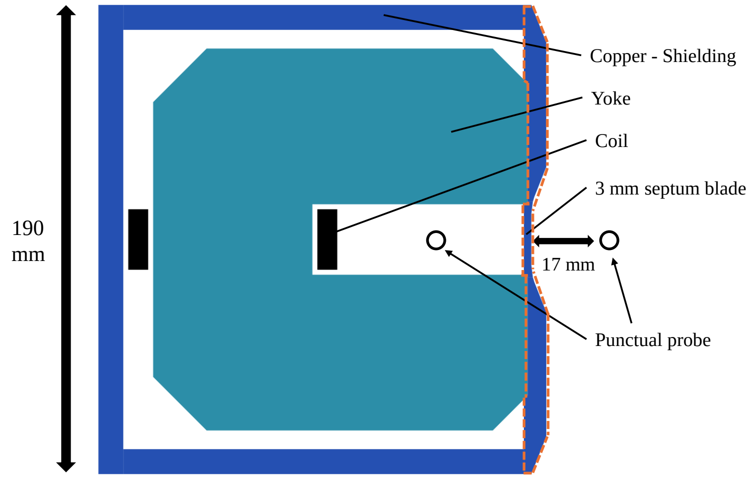

Fig. 4.1: **SMH16-CF cross-section**
A punctual probe is positioned both in the main field gap and 17 mm away from the septum blade. The material of the area that is marked by an orange dotted line is copper in a first measurement and aluminum in a second.

Figure 4.2 shows the longitudinal cross-section of the magnet and the positioning of the punctual probe. It is put at a distance of 17 mm next to the septum blade (as close as possible) and is moved along the longitudinal axis to capture the dependence of the leakage field on the position. Starting from the magnet's center, the probe is first moved towards the end of the magnet in steps of 100 mm. Near the end, the step size is decreased to 30 mm as a gradient of the leakage field is expected in this region. This is due to the increasing distance from the coil that produces the magnetic field. Moreover, the main magnetic field is measured by putting the probe into the aperture for the injected beam.

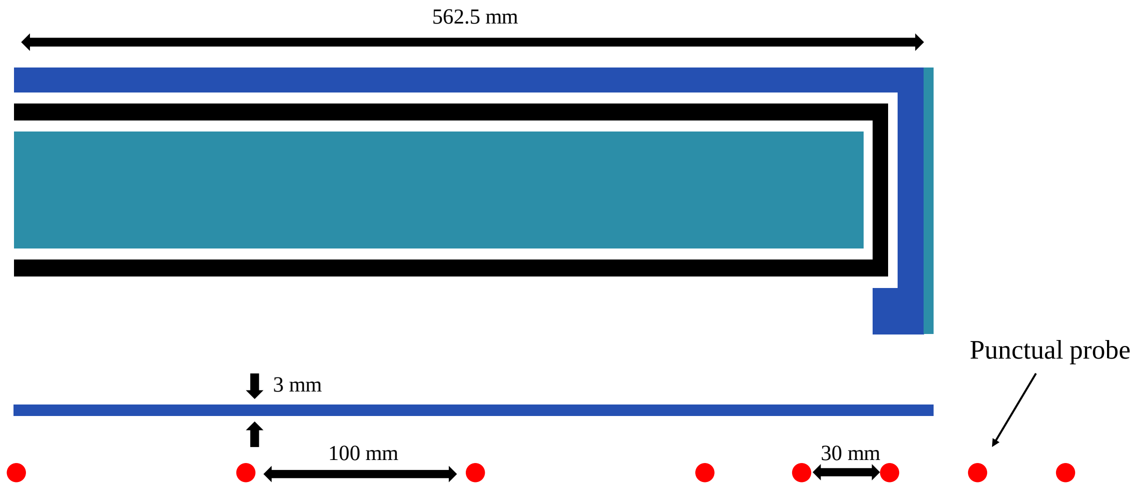

Fig. 4.2: SMH16-CF longitudinal cross-section and positioning of the punctual probe to perform a leakage field scan - only half of the magnet is measured

Current

The measurement of the current is displayed in Fig. 4.3 and shows a half sine pulse with a pulse width of around 640 μs and a peak current of 4976 Amperes. This is an average over all the pulses that were carried out at this frequency, since variations in the peak current of up 200 Amperes were observed. This current will be fed into the simulation software to obtain results for both the main and the leakage field to allow a comparison.

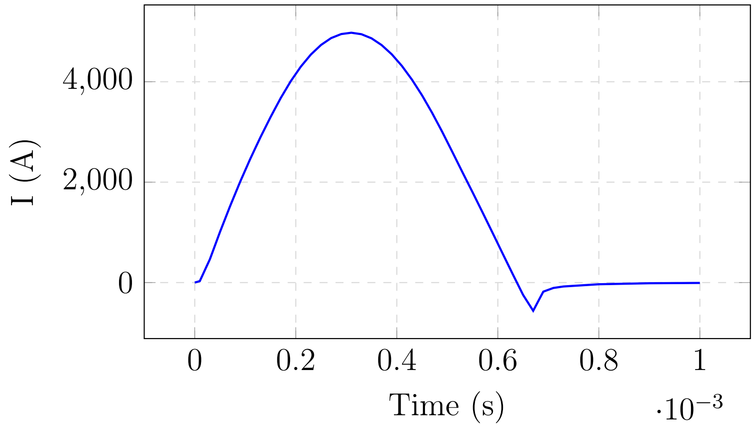

Fig. 4.3: **Current excitation of SMH16-CF**
640 μs half sine pulse with a peak current of 4976 Amperes

Main Field

Figure 4.4 compares the main magnetic field between simulation and measurement. The peak value of the magnetic field in the simulation is $B_{0,simu} = 207$ mT, which is about 2.47 % higher than the measured value of $B_{0,meas} = 202$ mT. A discussion of this and all the upcoming results will follow in Sec. 4.3.

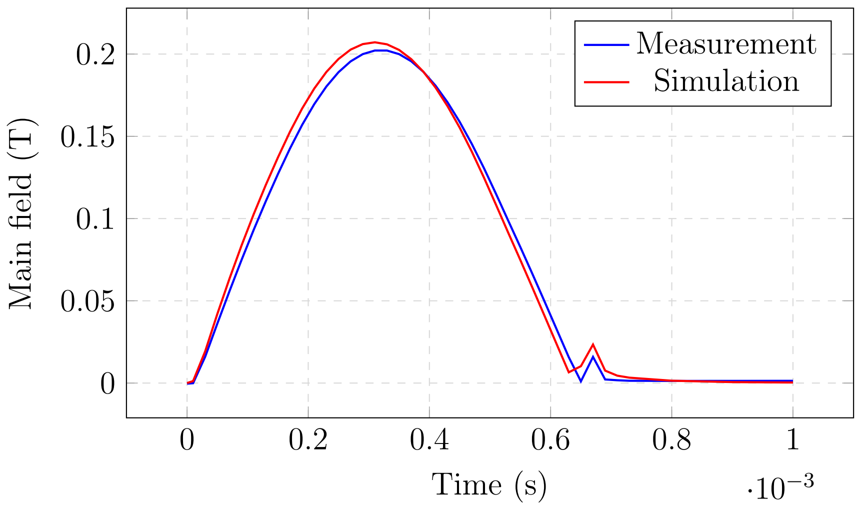

Fig. 4.4: Comparison between measurement and simulation of the main magnetic field of the SMH16-CF

Leakage Field

The leakage field is scanned by performing measurements at different locations along the longitudinal axis of the magnet, as explained in Sec. 4.1. A first measurement is performed with a copper septum blade and a second one using aluminum. The acquired data for the first measurement is shown in Fig. 4.5. Here, each line corresponds to a measurement at a given distance from the magnet's center. It can be observed that the highest leakage fields of around 5 mT occur in the center of the magnet, resulting in a ratio between the main field and the leakage field of around $\frac{B_{leak}}{B_{main}} = 2.5 \cdot 10^{-2}$, which is a good approximation for the ratio between the integrated field values. A comparison to the ratio $\frac{Bdl_{leak}}{Bdl_{main}} < 4 \cdot 10^{-5}$ for the SOLEIL II EC septum magnet, as was calculated in the previous chapter, shows again the benefits of two-layer shielding and fast, full-sine pulsing. The measurement also reflects the symmetry of SMH16-CF as the stray fields are rather homogeneous in the central part of the magnet. A decay of the field magnitude can be observed at the end of the magnet, which is 562.5 mm away from the magnet's center. This stands in contrast to the SOLEIL II eddy-current septum magnet of chapter 3. There, a decay of the leakage field was seen when going towards the downstream side of the magnet because of the decreasing septum thickness. This was shown in Sec. 3.3.

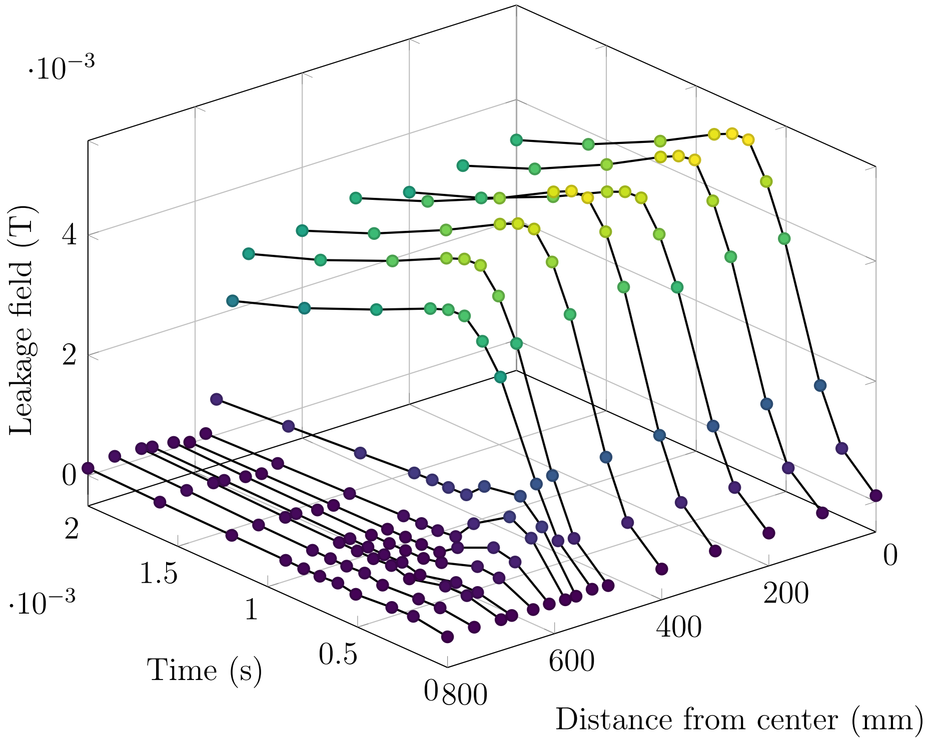

Fig. 4.5: **Measurement of the leakage field of SMH16-CF with a copper septum** Each line corresponds to one measurement of the magnetic field at one position along the longitudinal axis of the magnet.

The simulated leakage field is shown in Fig. 4.6. Here, one dotted line corresponds to one simulated time step that is reconstructed. Due to the symmetry of the magnet, only one three-dimensional simulation and one two-dimensional simulation is required to reconstruct the full three-dimensional model and its stray fields. Again, a homogeneous field can be seen in the center of the magnet with a decay at the end of the magnet at a distance from the center of about 500 mm.

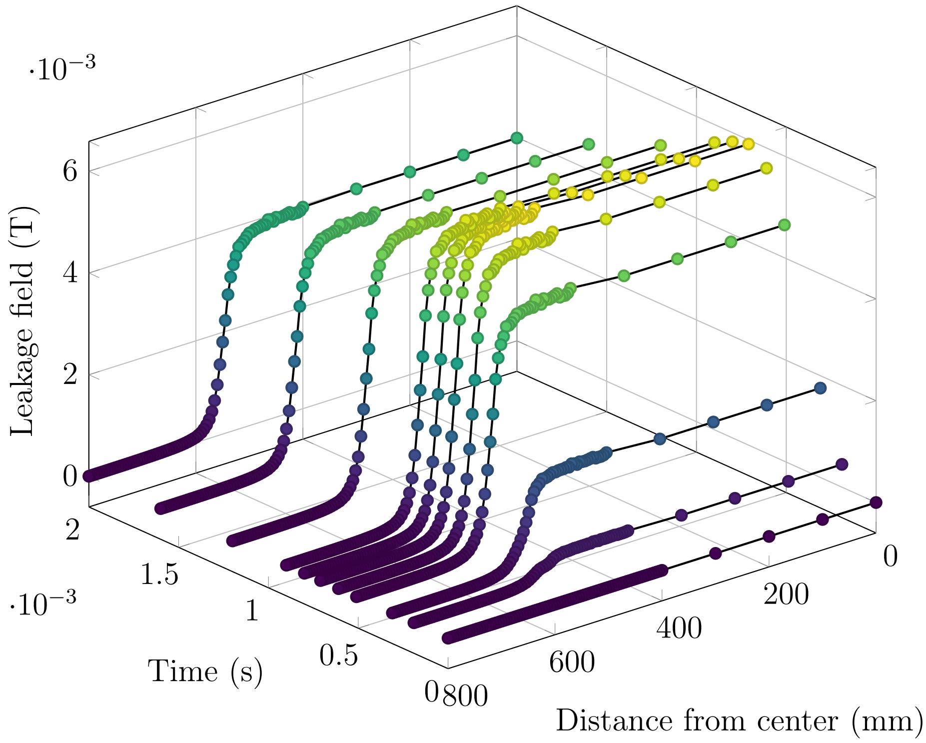

Fig. 4.6: **Simulation of the leakage field of SMH16-CF with a copper septum**
Each line corresponds to one simulated time step that is reconstructed from two-dimensional and three-dimensional simulations.

A direct comparison of the plots from Fig. 4.5 and Fig. 4.6 is difficult due to the amount of data-points. Therefore, the leakage field integral is chosen as the metric that is compared quantitatively. It is calculated using Eq. 2.4.2 for both the measurement and the simulation, the result of which is shown in Fig. 4.7. The leakage field reaches its peak value after about 700 μs. The simulated value for this peak is $Bdl_{leak,simu} = 3.52$ mTm and therefore around 34.4 % higher than the measured peak value of $Bdl_{leak,meas} = 2.62$ mTm. The simulated value remains higher than the measured value as the leakage fields decay after having reached its peak value. This decay is slow compared to the previous simulations due to the excitation with a half sine.

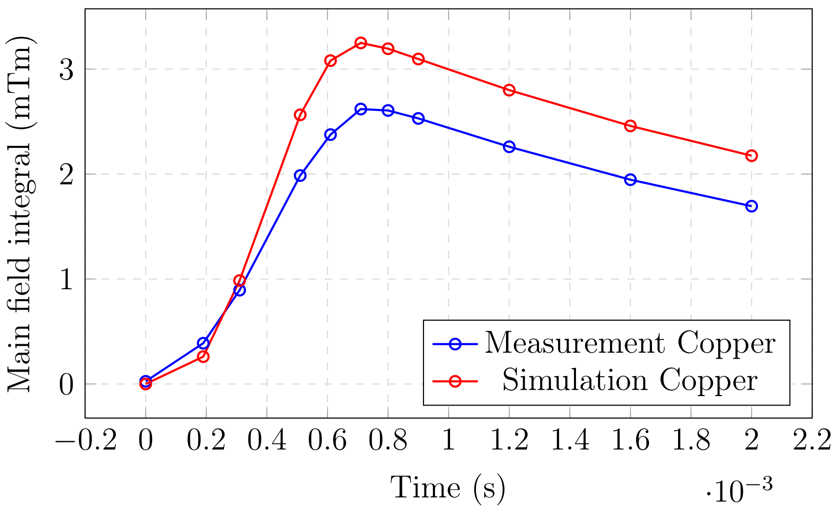

Fig. 4.7: Comparison of the leakage field integral of SMH16-CF with a copper septum blade between simulation and measurement

A second measurement is performed after substituting the copper septum blade by an aluminum blade. The figures showing the leakage field as a function of position and of time for measurement and simulation can be found in App. A in Fig. A.7 and Fig. A.8 respectively. The comparison between the leakage field integral as a function of time is depicted in Fig. 4.8. In this case, the peak value of the leakage field integral is reached after about 600 μs. The peak value for the simulation is $Bdl_{leak,simu} = 5.04$ mTm, which is about 22 % lower than the measured value of $Bdl_{leak,meas} = 6.52$ mTm. The increase of the leakage field integral for an aluminum septum blade compared to a copper septum blade is caused by the lower conductivity of aluminum.

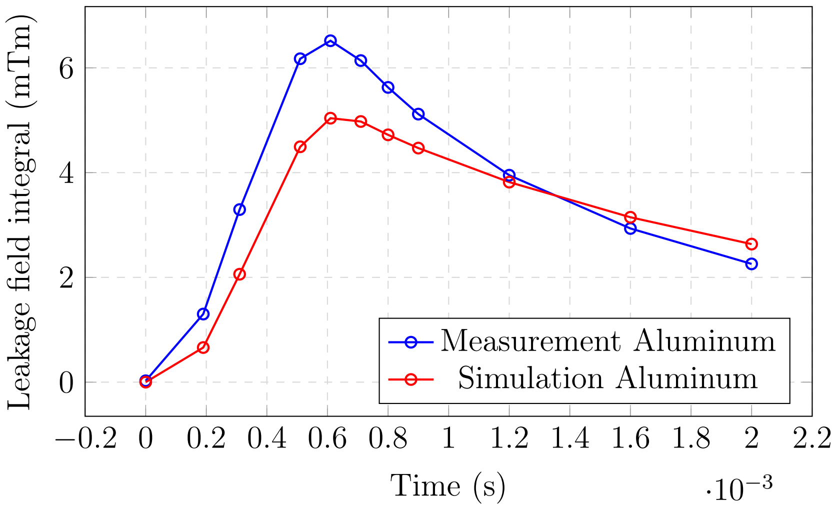

Fig. 4.8: Comparison of the leakage field integral of SMH16-CF with an aluminum septum blade between simulation and measurement

4.2 SOLEIL I - Spare Eddy-Current Septum Magnet

The second magnet that is magnetically measured is the spare septum magnet for the current injection scheme of the SOLEIL accelerator. The two cross-sections of the magnet can be viewed in Fig. 4.9 and in Fig. 4.10. The septum magnet has a length of around 650 mm, a gap height for the deflection field of 15 mm and a copper septum blade with a thickness of 3 mm. The measurements are provided by the Division Accélérateurs et Ingénierie of SOLEIL [5]. Here, the leakage field measurement is obtained with an integral probe that directly measures the leakage field integral. This integral probe comprises two connected copper wires that are stretched alongside the septum blade. The distance between the two copper wires is $w_{IP} = 0.5$ mm and the distance between the center of the integral probe and the septum blade is 3 mm [5]. Again, a voltage is induced in the wires due to time-varying magnetic fields and the leakage field integral can be calculated by integrating the induced voltage and dividing by the width w_{IP}:

$$Bdl(t) = \frac{1}{w_{IP}} \int_{t_{start}}^{t} U_{ind}(\tilde{t}) d\tilde{t} \tag{4.2.1}$$

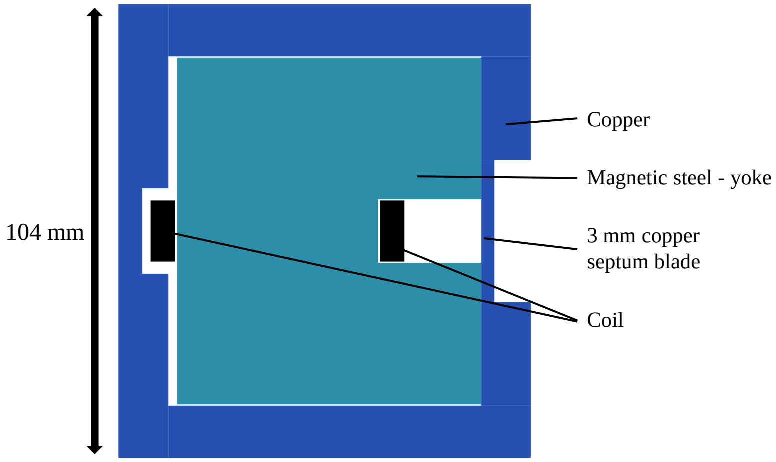

Fig. 4.9: Cross-section of the SOLEIL I spare septum magnet

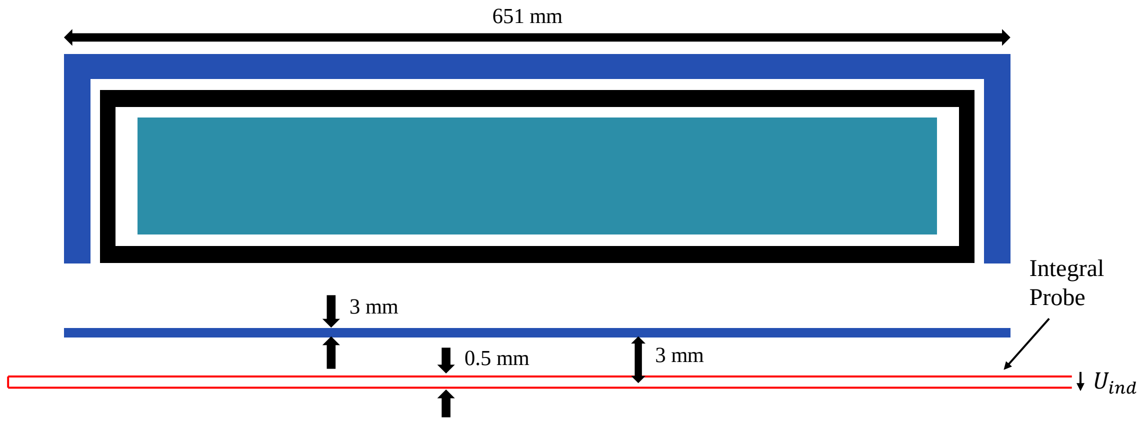

Fig. 4.10: SOLEIL spare septum magnet longitudinal cross-section and positioning of the integral probe to perform a leakage field measurement

Current

The SOLEIL I spare septum magnet is pulsed by a power converter that produces a full-sine excitation with a pulse width of 140 μs and a peak current of 4921 Amperes, as is shown in Fig. 4.11.

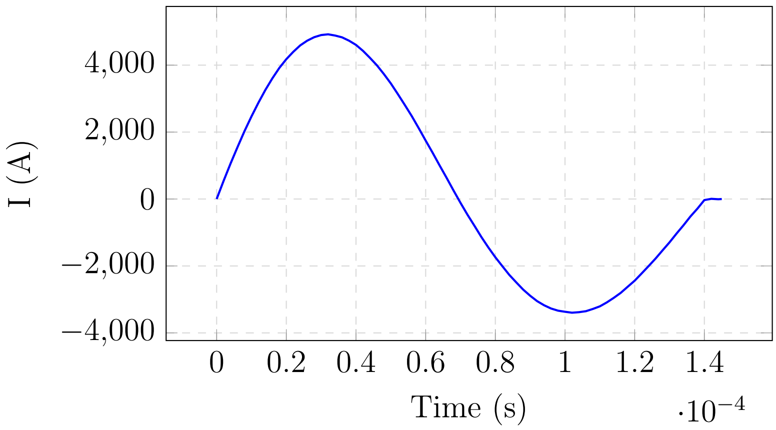

Fig. 4.11: **Current excitation of the SOLEIL eddy-current spare magnet** 140 μs full sine pulse with a peak current of 4921 Amperes

Table 4.1: **Comparison between measurement and simulation**
The table shows the peak values of simulation (S) and measurement (M) for different magnets and different excitations. SMH16-CF is pulsed with a half sine pulse (T/2) and the SOLEIL spare septum magnet with a full sine (T).

		Main field (mT)	Relative error (%)	Leakage field integral (mTm)	Relative error (%)
SMH16-CF Copper	M	202	2.48	2.62	34.4
$T/2 = 640$ μs, $I_{max} = 4976$ A	S	207		3.52	
SMH16-CF Aluminum	M			6.52	22.3
$T/2 = 640$ μs, $I_{max} = 4976$ A	S			5.04	
SOLEIL spare septum magnet	M			2.34	11.1
$T = 140$ μs, $I_{max} = 4921$ A	S			2.08	

Leakage Field

The results of the measurement of the leakage field integral using an integral probe as well as the simulated results are shown in Fig. 4.12. Here, the peak of the leakage field is reached after about 134 μs in the measurement and after 145 μs in the simulation. The peak values lie at $Bdl_{leak,meas} = 2.34$ mTm and $Bd_{leak,simu} = 2.08$ mTm respectively, resulting in a relative error of 11.1 %.

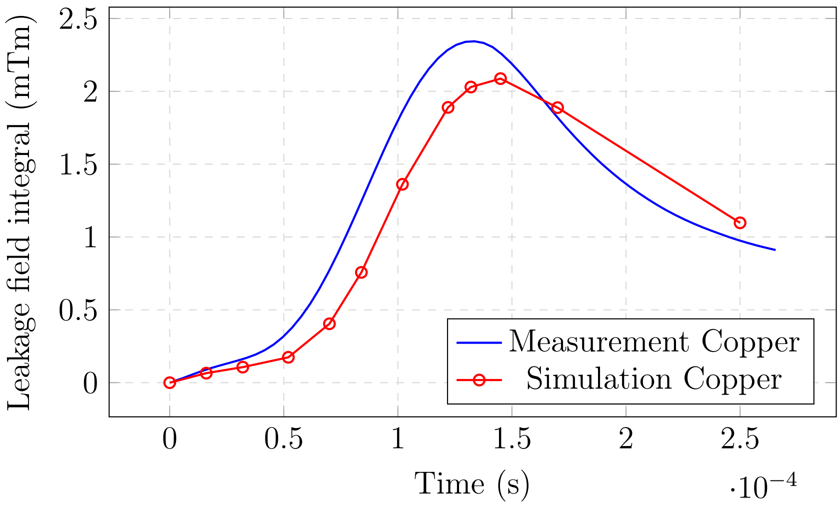

Fig. 4.12: Comparison of the leakage field integral between measurement and simulation for the SOLEIL spare septum magnet

4.3 Benchmarking - Discussion

The main results of this chapter are shown in Tab. 4.1. The simulations deviate from the measurements by up to around 35 %. This section is aimed at discussing these results and finding potential reasons for the observed deviations.
The variations between the measured and the simulated value for leakage field measurements are predominantly caused by the low fields that are being measured. The measurements are easily influenced and altered by potential other factors. Firstly, magnetic noise of other currents in proximity to the testing area may be captured by the magnetic probe. Especially the connecting cables that carry the current from the power converter to the septum magnet may cause magnetic noise, even though they were placed to minimize dis-

turbances. Secondly, both magnetic probes that were used average the magnetic field over the area that is enclosed by the measurement coil. This causes an error as the magnetic field decays roughly as $\frac{1}{d}$, with d referring to the distance to the septum blade. Furthermore, the position of the punctual probe in Sec. 4.1 was determined manually with a ruler measurement and a corresponding precision of $\pm$ 2 mm. The positioning of the integral probe in Sec. 4.2, however, was managed by an automatized measurement-bench, which can explain the better alignment for this measurement. Next, the power converter used in Sec. 4.1 to generate a half-sine pulse with a pulse width of 640 μs showed some significant variations in the current that it generated. Therefore, each punctual measurement was obtained with a current that varied up to 4 %, whereas all simulations were carried out using the same current. Finally, the bandwidth and transfer function of the probe itself can affect the results.

The simulations on the other hand use the literature values for the material properties of copper, aluminum and ferromagnetic steel. These might, however, differ slightly from the real values. Additionally, eddy-currents in the ferromagnetic yoke are neglected in the simulation as the yoke is laminated, which means that the yoke consists of many layers of ferromagnetic steel with insulation between them to prevent the flow of eddy-currents. This, however, doesn't stop the flow of eddy-currents perfectly, which can explain why the measured main field is slightly lower than the simulated main field.

Finally, it should be noted that an alignment for the leakage field measurements with the theoretical values of around 20 - 30 % is usually encountered for these kinds of measurements. Further investigation is required to close the gap between simulation and measurement, especially as a potential magnetic validation of the simulations that were carried out in chapter 3 would require an accuracy to the micro-Tesla level.

5 Conclusion and Outlook

In the following, the results of the simulations for the SOLEIL II eddy-current septum magnet from chapter 3 and the agreement between simulation and measurement as seen in chapter 4 are discussed.

Chapter 3 showed how the proposed design of the septum magnet meets the requirements that were set in Sec. 3.1. These requirements ensure that the beam dynamics of both the injected beam and the stored beam are as expected to guarantee a stable operation of the SOLEIL II accelerator.
First, the main field homogeneity was optimized by adding shims to the magnetic poles and a uniformity exceeding 0.1 % was achieved theoretically. The required dimensions of the shim were calculated to be in the order of hundreds of micro-meters. This can pose a challenge for the mechanical assembly and the real uniformity will ultimately be limited by the precision of construction.
Next, a simulation approach was established to deal with large model sizes and impractical simulation run times caused by skin-depths on the micrometer scale. This approach involved the reconstruction of the complete septum magnet with a set of smaller simulations. It has been validated and can potentially be utilized for other upcoming large models, until computing resources are improved. Using this approach, three different septum blades have been analyzed with respect to their shielding performance. A two layer septum blade consisting of a tapered layer of copper (thickness 3 mm to 0.5 mm) and a second ferromagnetic layer of μ-metal (0.5 mm) has been shown to provide sufficient shielding. The obtained value for the leakage field integral is $Bdl_{leak,DP} < 10$ μTm for a main field integral of 257 mTm for a peak excitation current of 4 kA. This shielding performance is achieved by the fast pulsing and the high permeability of μ-metal, which augment the induction of eddy-currents in the septum blade. However, a more detailed analysis of μ-metal is needed to determine its permeability and hysteresis curve at excitation frequencies above 1 kHz.

In chapter 4, magnetic tests were carried out to validate the simulations. A difference of 2.5 % between simulation and measurement has been observed for the main field, whereas the deviation for leakage field measurements went up to 35 %. Potential reasons for these deviations were discussed in Sec. 4.3. The measurement of small magnetic fields with gradients poses a challenge for validating septum magnets, as previous measurements at CERN showed similar alignment between measurement and simulation. Nevertheless, the simulations provide a good understanding of the leakage field and a decent approximation for both the order of magnitude and the transient behavior of the stray fields. Further investigation is needed to close the gap between simulation and measurement.
The proposed design has been validated and a compromise between pulse frequency and magnetic shielding has been found.
The magnet and its pulse generator will finally be assembled in the upcoming year and their true performance will ultimately be determined by the behavior of the particle beam in the SOLEIL II accelerator.

A Appendix

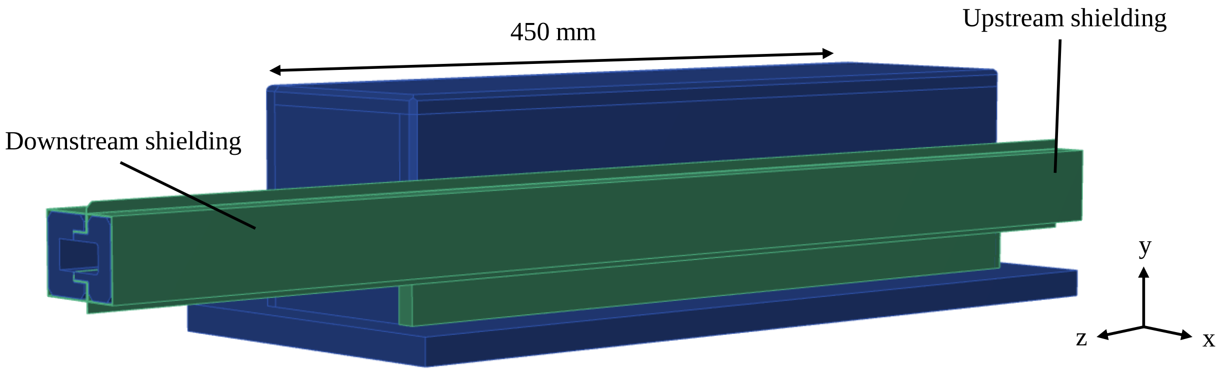

Fig. A.1: **A complete three-dimensional view of the SOLEIL II eddy-current septum magnet**
The injected beam and the stored beam enter the septum magnet on the upstream side. The injected beam is deflected towards the stored beam.

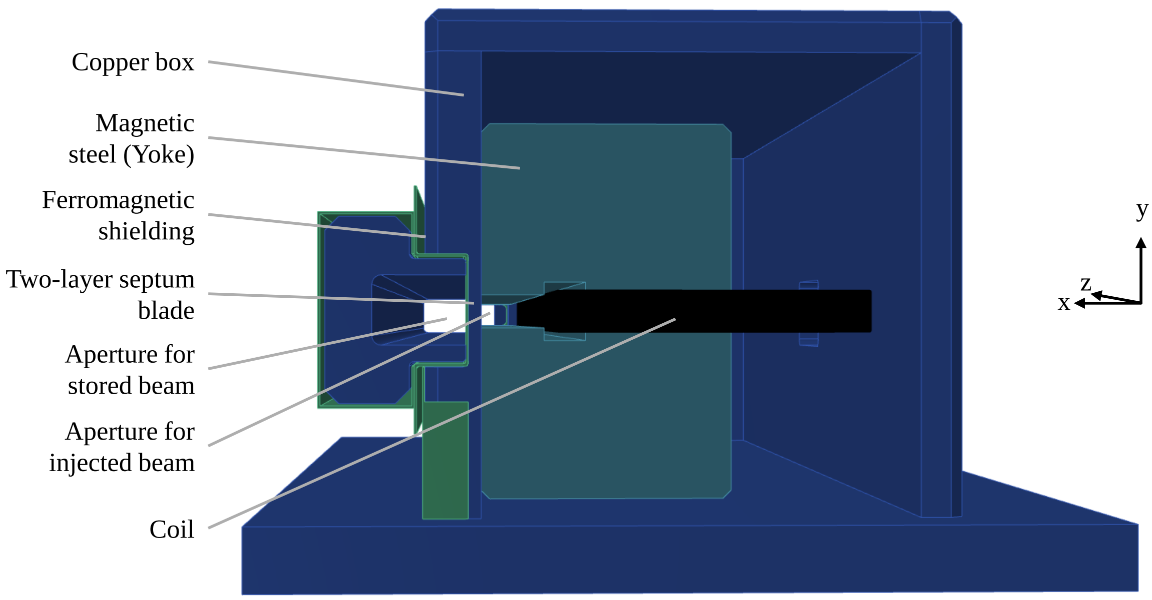

Fig. A.2: Three-dimensional view of the cross-section of the SOLEIL II eddy-current septum magnet

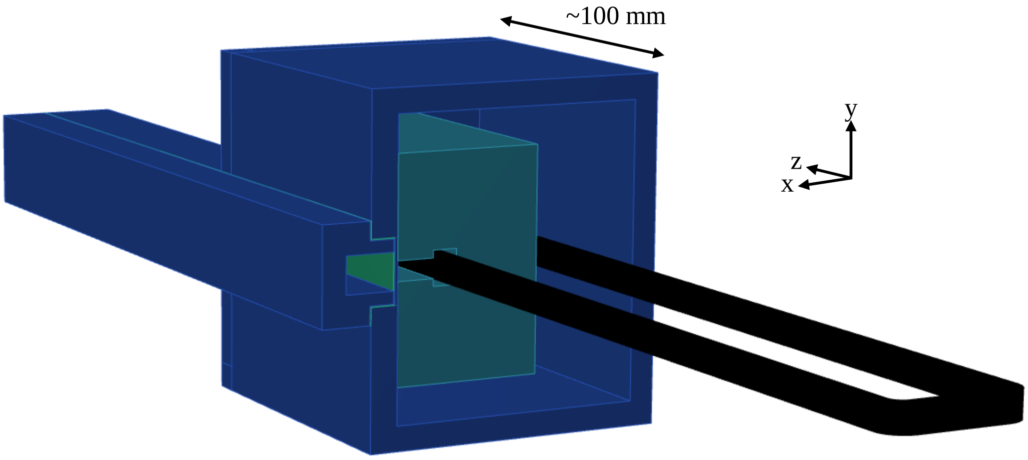

Fig. A.3: **Three-dimensional model for the upstream end of the SOLEIL II eddy-current septum magnet**
The cutting-plane is perpendicular to the coil. Therefore, the boundary condition "tangential magnetic field" is imposed on all faces at the cutting-plane. The coil is not part of the mesh and is therefore kept entirely.

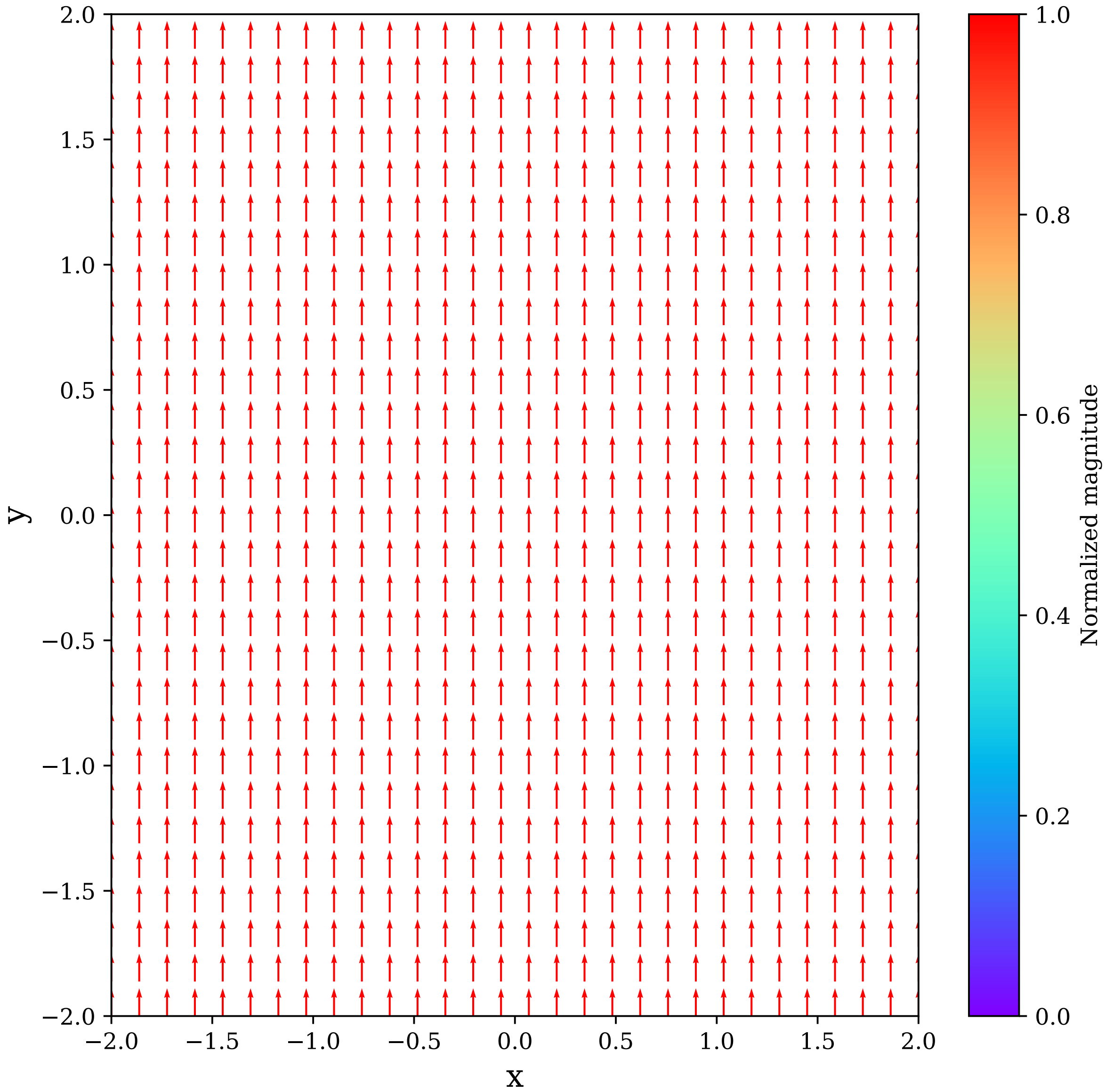

Fig. A.4: **Magnetic dipole**
The two-dimensional magnetic field of a dipole is shwon: $\vec{B}(x, y) = (0, 1)^T$. The magnitude of the magnetic field, indicated by the color, is normalized by the maximum value.

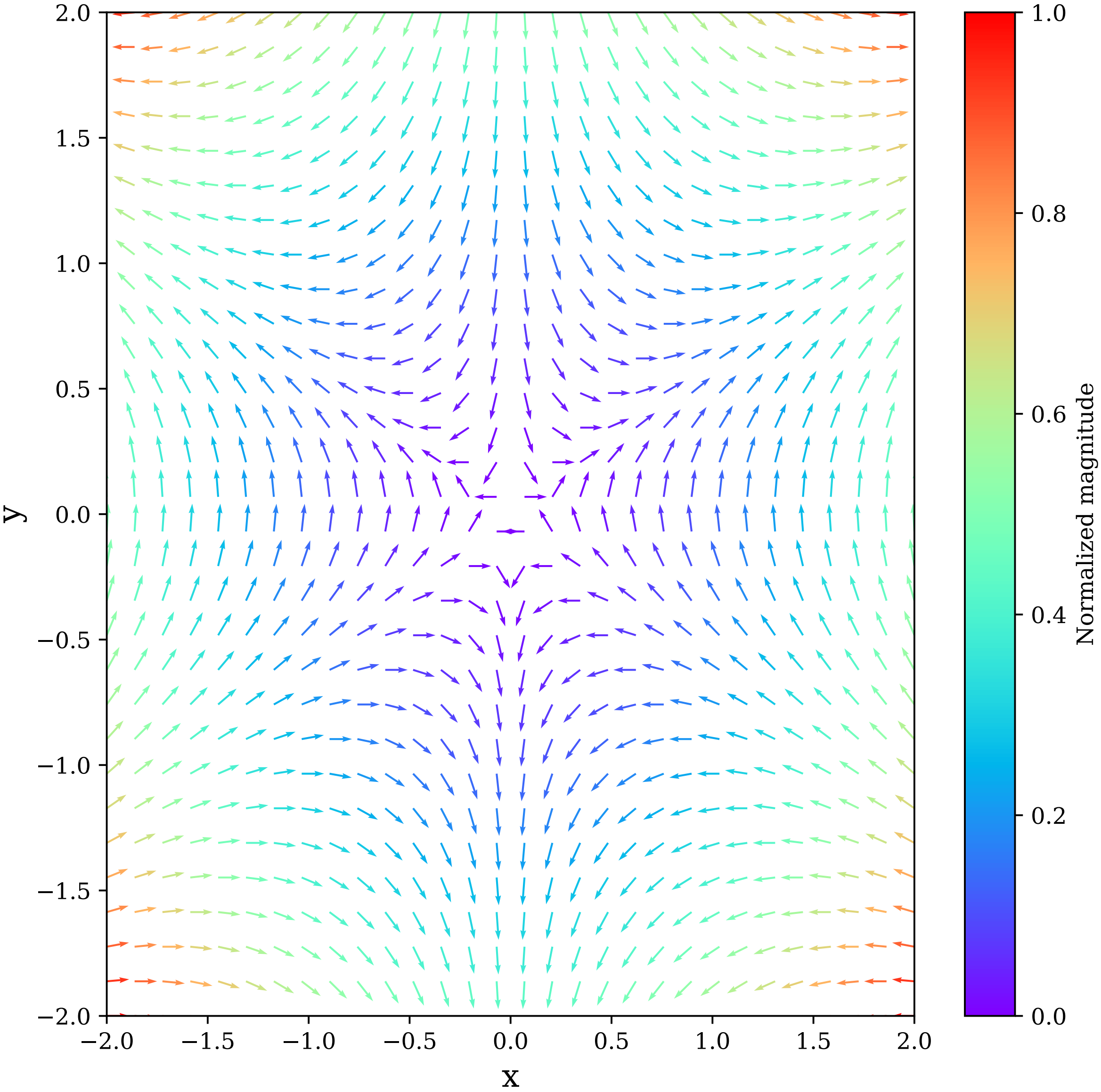

Fig. A.5: **Magnetic sextupole**
The two-dimensional magnetic field of a sextupole is shown: $\vec{B}(x, y) = (2xy, x^2 - y^2)^T$. The magnitude of the magnetic field, indicated by the color, is normalized by the maximum value.

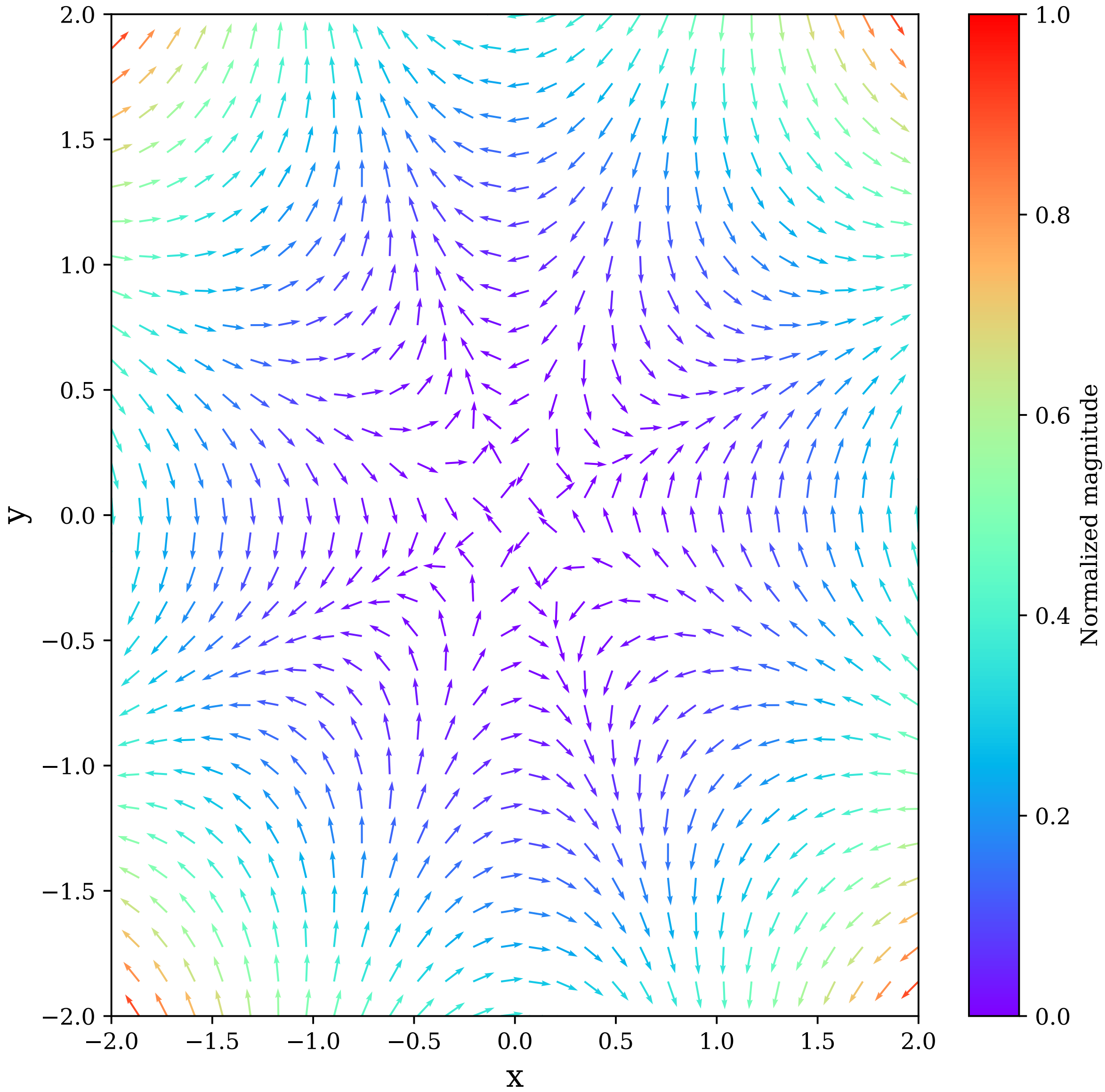

Fig. A.6: **Magnetic octupole**
The two-dimensional magnetic field of an octupole is shown: $\vec{B}(x,y) = (3yx^2 - y^3, x^3 - 3xy^2)^T$. The magnitude of the magnetic field, indicated by the color, is normalized by the maximum value.

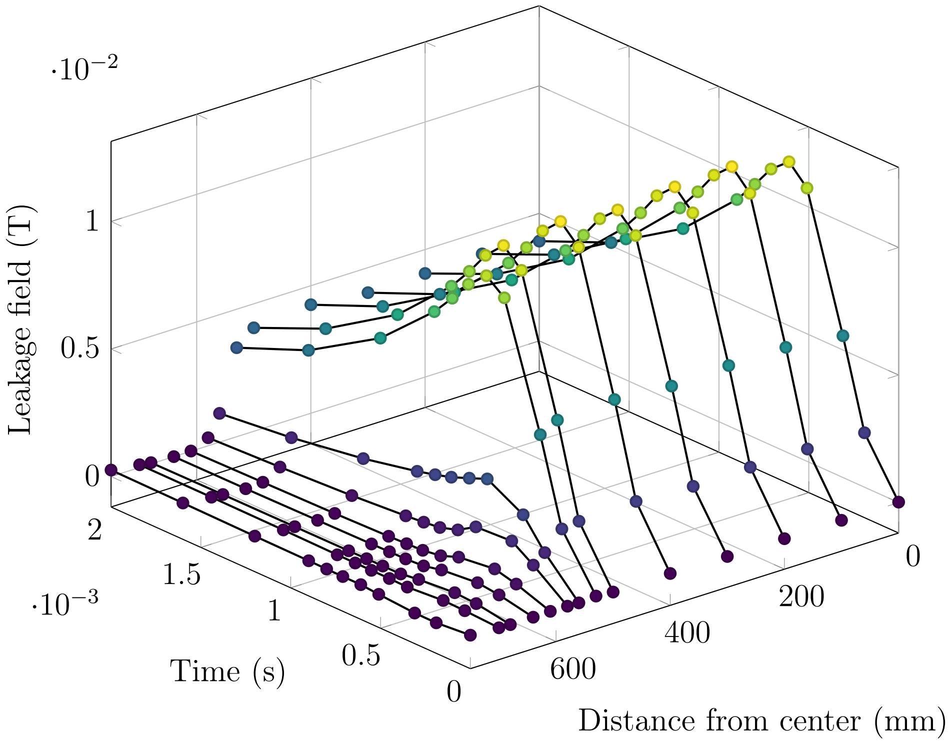

Fig. A.7: **Measurement of the leakage field of SMH16-CF with an aluminum septum**
Each line corresponds to one measurement of the magnetic field at one position along the longitudinal axis of the magnet.

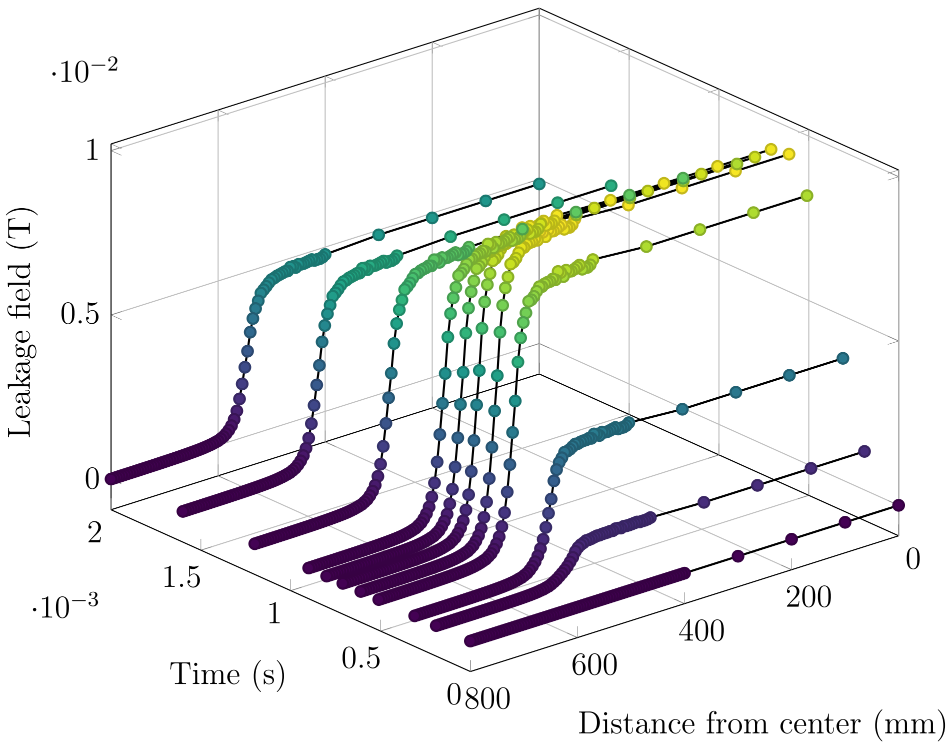

Fig. A.8: **Simulation of the leakage field of SMH16-CF with an aluminum septum**
Each line corresponds to one simulated time step that is reconstructed from two-dimensional and three-dimensional simulations.

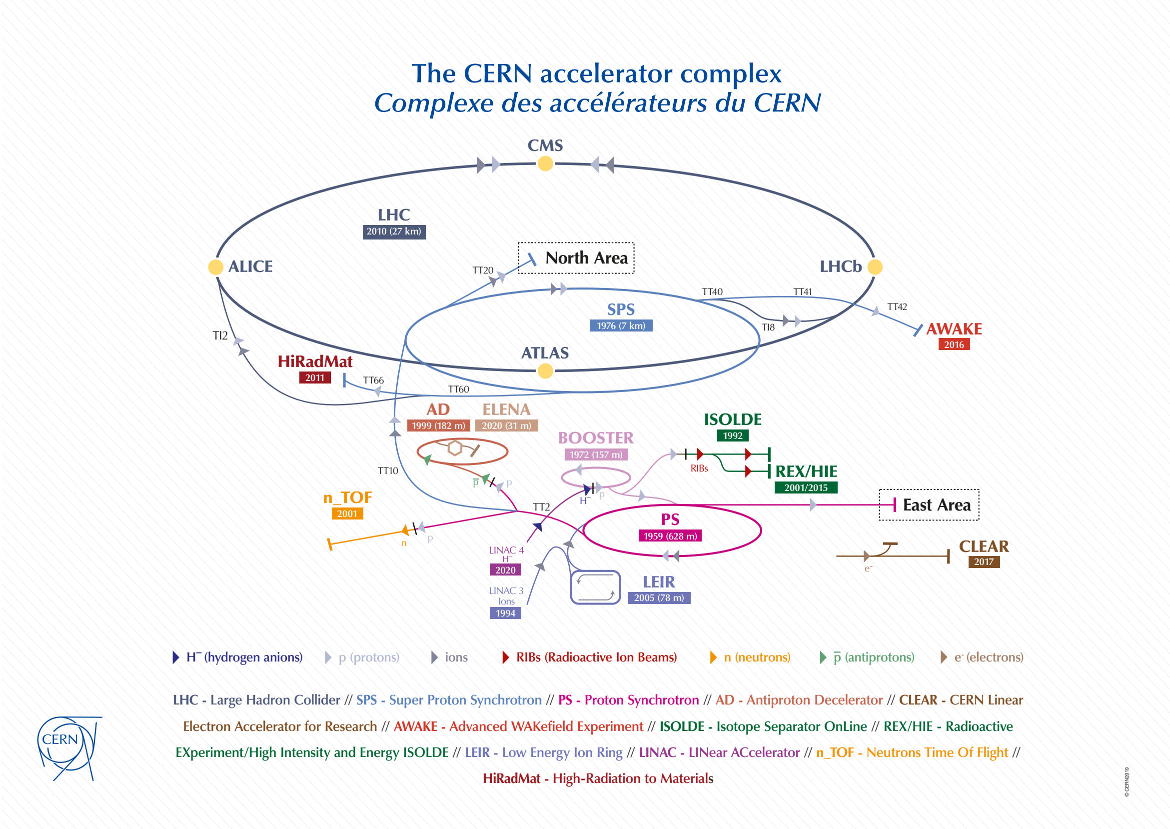

Fig. A.9: CERN accelerator complex [1]

Bibliography

[1] CERN website. [Online]. Available: https://home.cern/science/accelerators/accelerator-complex/panoramas

[2] SOLEIL website. [Online]. Available: https://www.synchrotron-soleil.fr/fr/recherche

[3] P. Alexandre, R. B. E. Fekih, A. Letrésor, S. Thoraud, J. da Silva Castro, F. Bouvet, J. Breunlin, Åke Andersson, and P. Fernandes Tavares, "Transparent top-up injection into a fourth-generation storage ring," *Nuclear Instruments and Methods in Physics Research Section A: Accelerators, Spectrometers, Detectors and Associated Equipment*, vol. 986, p. 164739, 2021. [Online]. Available: https://www.sciencedirect.com/science/article/pii/S0168900220311360

[4] M. Barnes, J. Borburgh, B. Goddard, and M. Hourican, "Injection and extraction magnets: Septa," 06 2009.

[5] *Weekly discussions and communication with the Division Accélérateurs et Ingénierie of SOLEIL, in particular with Patrick Alexandre.*

[6] H. E. Knoepfel, *Magnetic Fields, A Comprehensive Theoretical Treatise for Practical Use.* John Wiley and SONS, INC., 2000.

[7] *DI-MAX® M-10X NON-ORIENTED ELECTRICAL STEELS, PRELIMINARY PRODUCT DATA BULLETIN*, AK Steel Corporation, West Chester, Ohio, USA.

[8] H. Felice, S. P. P. Ferracin, and E. Todesco, "Superconducting accelerator magnets - unit 5: Field harmonics," in *USPAS*, 2012.

[9] S. Turner, Ed., *CAS - CERN Accelerator School: Magnetic measurement and alignment*, ser. CERN Accelerator School, CERN Yellow Reports: School Proceedings, no. CERN-92-05, CERN Accelerator School. Geneva: CERN, Mar 1992, cC-BY-3.0 license.

[10] H. Wiedemann, *Particle Accelerator Physics, Third Edition.* Springer, 2007.

[11] *Opera-3d User Guide, Version 2024 SP1.* Dassault Systèmes, 2023.

[12] J. T. Tanabe, *Iron Dominated Electromagnets.* World Scientific Publishing Co. Pte. Ltd., 2005.

[13] R. A. Serway, *Principles of physics.* Fort Worth : Saunders College Pub, 1998.

[14] P. Arpaia, P. N. Burrows, M. Buzio, C. Gohil, M. Pentella, and D. Schulte, "Magnetic characterization of mumetal® for passive shielding of stray fields down to the nano-tesla level," *Nuclear Instruments and Methods in Physics Research Section A: Accelerators, Spectrometers, Detectors and Associated Equipment*, vol. 988, p. 164904, 2021. [Online]. Available: https://www.sciencedirect.com/science/article/pii/S0168900220313012

[15] *Additional Support Knowledgebase, Version 2024 SP1.* Dassault Systèmes, 2023.

[16] *Private communication with Miroslav Atanasov (CERN SY-ABT-SE).*

[17] T. Helseth, M. Atanasov, B. Balhan, J. Borburgh, L. Ducimetière, M. R. Fraser, and T. Kramer, "Feasibility study for the novel CERN PS fast extraction septum," 2021. [Online]. Available: https://api.semanticscholar.org/CorpusID:240632011

[18] D. Shuman, W. Barry, S. Prestemon, R. Schlueter, C. Steier, and G. Stover, "Stray field reduction of als eddy current septum magnets," in *Proceedings of the 2005 Particle Accelerator Conference*, 2005, pp. 3718–3720.

[19] K. V. Sathish, N. Sowmya, R. Munirathnam, H. C. Manjunatha, L. Seenappa, and K. N. Sridhar, "Radiation shielding properties of aluminium alloys," *Radiation Effects and Defects in Solids*, vol. 178, no. 9-10, pp. 1301–1320, 2023. [Online]. Available: https://doi.org/10.1080/10420150.2023.2249180